Numerical Study of Turbidity Current over a Three-Dimensional Seafloor

Ching Hao Yu[1], Liang Zhao[2], Haw Liang Wen[3],
Tony Wen Hann Sheu[3,4,*] and Rui Dong An[1,*]

[1] *State key lab of Hydraulics and Mountain River Engineering, Sichuan University, Sichuan 610000, P.R. China.*
[2] *Ocean College, Zhejiang University, Hangzhou 310000, P.R. China.*
[3] *Department of Engineering Science and Ocean Engineering, National Taiwan University, Taipei, R. O. China.*
[4] *Institute of Applied Mathematical Sciences, National Taiwan University, Taipei, R. O. China.*

Abstract. Turbidity current over a Gaussian-bump is investigated numerically using the upwinding combined compact difference (UCCD) scheme and the immersed boundary (IB) method in Cartesian grids. In the prediction of lock-exchange gravity-driven flow motion, the initial discontinuous concentration field is smoothed to avoid numerical oscillation by solving the Hamilton-Jacobi equation. The UCCD spatial scheme with sixth-order accuracy which introduces less dispersion errors is then used to discretize advection and diffusion terms in the calculation of concentration transport equation. Direct forcing IB method is employed to treat solid object bumps in the fluid flow. The incompressible Navier-Stokes solutions are obtained through the projection method. Analysis of the smoothing procedure, grid sensitivity and the effect of the Schmidt numbers is performed for the turbidity current problem to validate the proposed numerical algorithm, which is shown to be capable of accurately demonstrating their results. Finally, several problems of turbidity current over a three-dimensional seafloor are investigated. The front locations of the currents interacting with the bump are predicted under different Reynolds numbers. Also, the current properties, namely the suspended particle mass, sedimentation rate and energy budget, are compared with the available numerical results.

AMS subject classifications: 35Q30, 76D05, 76D27, 76M20

Key words: Turbidity current, upwinding combined compact difference scheme, immersed boundary method, concentration transport equation, sedimentation rates, energy budget.

Corresponding author. Email addresses: `twhsheu@ntu.edu.tw` (T. W. H. Sheu), `anruidong@scu.edu.cn` (R. D. An), `chyu@zju.edu.cn` (C. H. Yu), `liangz@zju.edu.cn` (L. Zhao), `luisleo52655@gmail.com` (H. L. Wen)

1   Introduction

The density difference between flow and its ambient environment results in the formation of gravity currents [1–4]. Among all types of gravity currents, turbidity current, has a tendency to be slowed down earlier due to settlement-induced energy loss of particles. Turbidity current is ubiquitous in various natural processes. For example, the turbidity currents flowing down continental shelves can suddenly release dense gases into the atmosphere. Besides, turbidity currents can interact with seafloors of various shapes, which may form complex topographical features including fans and lobes, gullies, levees and sediment waves [5–7]. Further investigation is needed to study the dynamical mechanism of turbidity currents.

Laboratory experiments have been conducted to investigate evolution of turbidity currents [8]. A high resolution scheme is then adopted to investigate gravity currents in a rectangular domain with a varying slope [9]. The lock-exchange gravity current propagating along a flat bottom is studied by a two-way coupled Euler-Lagrange model proposed by Chou et al. [10]. Their numerical simulations have revealed more detailed features of particle-laden flow concerning front location and deposited mass. For more information about the theoretical formulation and application of two-way coupled Euler-Lagrange models, one can refer to [11, 12]. Large Eddy Simulation (LES) is applied to study the evolution of gravity currents and its interaction with structures on complex 3-D seafloors under high Reynolds number conditions [13]. Direct Numerical Simulation (DNS) is also applied to investigate the interaction of turbidity currents with bumps of various shapes. Investigation shows that mixing of gravity currents with the ambient environment is not as intensive as that of turbidity currents because of the difference in particle settling velocity [5]. Refs. [14–18] discussed the features of turbidity current and its accompanying instability mechanism in detail using high resolution schemes.

High resolution schemes, i.e., ENO (Essentially non-oscillatory) and WENO (Weighted essentially non-oscillatory) [19, 20], usually adopt different nonlinear adaptive procedures to obtain locally smoothest stencils, to suppress numerical oscillations across physical discontinuities. It is well known that ENO and WENO schemes are over-dissipative in turbulence simulation because of the excessive dissipation introduced. Continuous efforts have been dedicated to WENO schemes to expand its application area. Latest development in WENO schemes can be found in [21].

Different from high resolution schemes, compact schemes receive in-depth investigation in DNS of Navier-Stokes simulation thanks to their advanced capability in providing high accuracy solutions [22]. Besides, compact schemes are less costly and more accurate than explicit finite difference schemes. Centered compact difference schemes were first proposed by Lele [23] in 1970s. However, due to its zero-dissipation property, centered compact difference schemes may induce high-frequency oscillations in smooth flow regions. In order to eliminate this high-frequency oscillation, artificial viscosity should be included. Upwind compact schemes contain inherent artificial viscosity, which makes it more stable than centered compact schemes [24–29]. It should be noted, however, that, it

may be premised that the introduced artificial viscosity should not be too large. Otherwise, it may smear genuine physical properties.

In order to predict fluid flows in regions bounded by complex geometry, the Immersive Boundary method (IB) is applicable to problems with irregular solid objects, and does not necessarily have to conform to Cartesian grids. Because grids do not conform to the solid boundary, proper boundaries should be imposed to carefully modify the governing equations around the boundary. Sheu et al. [30] developed an exact advection-diffusion-reaction scheme, which has already been successfully applied to get flow solutions in irregular domains using IB methods. Interpolation techniques have been proposed by some researchers to evaluate the momentum forcing term [31, 32]. However, application of polynomials in algebraic-based interpolations to treat boundaries may to a more or less extent induce numerical instabilities. Differential-based interpolations have been proposed to improve classical algebraic-based interpolations [33]. More examples using IB methods can be found in Refs. [34, 35].

The focus of this study is to smoothen the discontinuous initial concentration field by solving the Hamilton-Jacobi equation introduced in [36, 37]. Then, UCCD scheme [25] is adopted, which introduces less dispersion and dissipation errors into the formulation and thus enables simultaneously approximating both first and second derivatives in the concentration transport equation. Section 2 introduces the mathematical model including governing equations and immersed boundary methods. Section 3 presents the problem under investigation. Numerical methods of the turbidity current is presented in Section 4. Features of the turbidity current are discussed in Section 5, where comparison against predicted results of Nasr-Azadni and Meiburg [7] is also made. Energy budget is also discussed. Section 6 presents major conclusions drawn from this study.

2   Mathematical model

2.1   Governing equations

The motion of an incompressible viscous fluid flow under investigation is governed by the following three-dimensional dimensionless continuity and momentum equations [14, 38]

$$\nabla \cdot \mathbf{u} = 0, \tag{2.1}$$

$$\frac{\partial \mathbf{u}}{\partial t} + \mathbf{u} \cdot \nabla \mathbf{u} = -\nabla p + \frac{1}{Re}\nabla^2 \mathbf{u} + c\,\mathbf{e_g}. \tag{2.2}$$

In this elliptic-parabolic set of partial differential equations, u and p represent the dimensionless velocity vector and pressure, respectively. The vector $\mathbf{e_g}$ which is defined as $(0,0,-1)^{\mathbf{T}}$ denotes the unit vector in the direction of gravitational acceleration. The term $c\,\mathbf{e_g}$ in Eq. (2.2) is denoted as the buoyancy force vector derived from the assumption that the density difference between the particle-laden and clear fluid is minor. The Reynolds

number is defined as

$$Re = \frac{\hat{u}_b \hat{H}/2}{\hat{v}}, \tag{2.3}$$

where $\hat{v}$, $\hat{H}$ and $\hat{u}_b$ denote the kinematic viscosity coefficient, lock height and buoyancy velocity, respectively. The buoyancy velocity shown in Eq. (2.3) is defined as

$$\hat{u}_b = \sqrt{\frac{\hat{H}}{2} \frac{(\hat{\rho}_p - \hat{\rho}_0)C_r}{\hat{\rho}_0} \hat{g}}. \tag{2.4}$$

In Eq. (2.4), $\hat{\rho}_p$ and $\hat{\rho}_0$ are the particle density and the ambient fluid density, respectively. C_r denotes the fraction of particle volume in a cell at $t=0$. Note that parameters with the symbol "∧" are dimensional quantities in all the above equations.

As particles moving with the fluid velocity plus the Stokes settling velocity, the concentration fields for c_1 and c_2 evolve in Eulerian coordinates by

$$\frac{\partial c_i}{\partial t} + (u_i + u_s^i \mathbf{e_g}) \cdot \nabla c_i = \frac{1}{Sc_i Re} \nabla^2 c_i \quad i=1,2. \tag{2.5}$$

In the above equation, u_s^i and Sc_i ($= \frac{\hat{v}}{\hat{\kappa}_i}$; $i=1,2$) are the settling velocity of sediment in the gravitational direction and the Schmidt number, respectively. The field variable c_i ($i=1,2$) denotes the *ith* particle concentration which has been normalized by the total initial volume fraction C_r of the particles

$$c_i = \frac{C_i}{C_r}, \quad i=1,2. \tag{2.6}$$

The total concentration c given below is the sum of c_i at all the computed locations

$$c = \sum_{i=1}^{2} c_i. \tag{2.7}$$

In Eq. (2.6), C_i represents the particle concentration field. The particle inertia and particle-particle interaction are negligibly small in the gravitational direction. It is implied that the sediment is suspended in the ambient fluid. In line with the physical laws, particles shall move along with the flow. Also, the Stokes settling velocity can be defined as

$$u_s = \frac{\hat{d}_p^2 (\hat{\rho}_p - \hat{\rho})\hat{g}}{18\hat{\mu}}. \tag{2.8}$$

It should be kept in mind that the particle settling velocity results from the balance between the gravitational force and the Stokes drag force over a sphere in a flow of uniform velocity. The above Stokes settling velocity u_s is the function of particle diameter $\hat{d}_p$ and dynamic viscosity coefficient $\hat{\mu}$. Settling velocities on fine particles ($u_s^1 = 0.006$) and coarse particles ($u_s^2 = 0.03$) are prescribed differently. Schmidt number Sc_i describes the ratio of the kinematic viscosity $\hat{v}$ to the molecular diffusion coefficient $\hat{\kappa}$, whose effect on the dynamics of fluid flow can be ignored when $Sc_i \geq \mathcal{O}(1)$. The Schmidt number is therefore set to have the value of unity in this study [7].

2.2   Direct forcing Immersed Boundary (IB) method

First of all, the interface-grid relation should be established using the given immersed boundary description, which can be a parametric curve, surface or triangulation. On this basis, all the grid points can be classified into three categories, i.e., fluid points, forcing points, and solid points. Fluid points refer to the points in the fluid phase, forcing points refer to the points in the fluid phase with a few neighboring points in the solid phase, and solid points refer to the grid points within the solid structure (See Fig. 1). The Navier-Stokes solver is universally applicable to all the three categories of grid points. The force exerted by the structure on the fluid, represented as a forcing vector $\mathbf{f}_i^{n+1}$, is introduced as a source term in the momentum equation to simulate the effect of immersed boundary on the flow field:

$$\frac{\partial \mathbf{u}}{\partial t} + \mathbf{u} \cdot \nabla \mathbf{u} = -\nabla p + \frac{1}{Re} \nabla^2 \mathbf{u} + c \, \mathbf{e_g} + \mathbf{f}_i^{n+1}. \tag{2.9}$$

The forcing vector in Eq. (2.9) can be evaluated in the following way. First, use the explicit forward Euler scheme to solve the provisional velocity field $\tilde{\mathbf{u}}_i$ for $\hat{\mathbf{u}}_i$ in the following equation

$$\frac{\hat{\mathbf{u}}_i - \mathbf{u}_i^n}{\Delta t} + \mathbf{u}_i^n \cdot \nabla \mathbf{u}_i^n = -\nabla p_i^n + \frac{1}{Re} \nabla^2 \mathbf{u}_i^n + c_i^n \, \mathbf{e_g}. \tag{2.10}$$
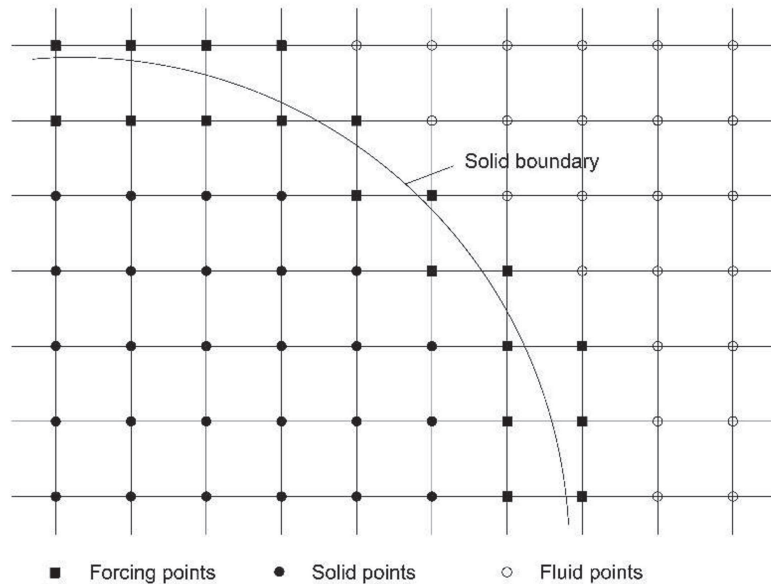

Figure 1: Grid classification for the forcing, fluid and solid points.

Following this, substitute the $\hat{\mathbf{u}}_i$ with $\mathbf{u}_f$ in Eq. (2.10) to directly derive the forcing function $\mathbf{f}_i^{n+1}$:

$$\mathbf{f}_i^{n+1} = \frac{\hat{\mathbf{u}}_f - \mathbf{u}_i^n}{\Delta t} + \mathbf{u}_i^n \cdot \nabla \mathbf{u}_i^n + \nabla p_i^n - \frac{1}{Re} \nabla^2 \mathbf{u}_i^n - c_i^n \, \mathbf{e_g}. \tag{2.11}$$

This forcing is direct because the desired velocity is prescribed on the boundary in prior. When the interface and the forcing points happen to coincide, then $\hat{\mathbf{u}}_f$ is the prescribed velocity boundary condition and the prescribed or predicted local velocity of the immersed body. Usually, the grid points and the moving interface can hardly coincide, and the $\mathbf{f}_i^{n+1}$ has to be computed using the given information. One can adopt the linear interpolation scheme presented in Ref. [33]. In fact, no interpolation is needed in our study, and the geometry is described in a percentage of the solid volume way [39]. Detailed algorithm of IB method in this study described in Section 4.3 can be seen.

3 Problem description and boundary condition

3.1 Problem description

The dam-break flow resulting from removal of the lock as shown in Fig. 2 will impound the fresh water reservoir, thereby resulting in a flood over the Gauss-bump under investigation. The parameters are tabulated in Table 1 for all simulation cases. For the **FL**, **B1** and **B2** cases, the same lock and the same dimensionless settling velocity ($u_s^1 = 0.03$ for coarse particles and $u_s^2 = 0.006$ for fine particles) are considered. There is no bump in the downstream end in the **FL** case while the bump height is 0.25 and 0.5 for the case **B1** and **B2**, respectively. The cases **B2−GC1** have the same parameters as those of the case **B2**, except that the settling velocity in cases **B2−GC1** is zero. The cases **B2−GC1** are simulated to observe the difference between gravity and turbidity currents.

Table 1: Parameters for the five simulation cases.

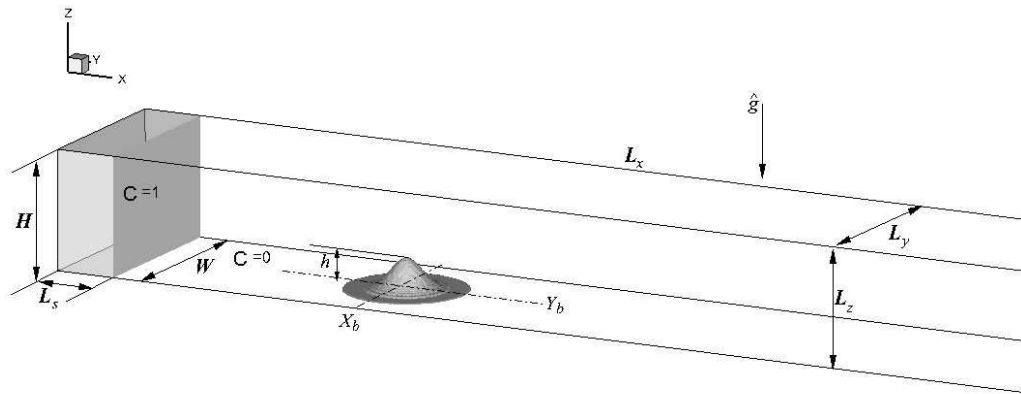| Name	Shape	Bump height(h)	Re	Number of grid points (N_x, N_y, N_z)	Domain size (L_x, L_y, L_z)	Lock-dimensions (L_s, H, W)
FL	Flat	0	2000	(760,40,60)	(38,2,3)	(1,2,3)
B1	Bump	0.25	2000	(760,40,60)	(38,2,3)	(1,2,3)
B2	Bump	0.5	2000	(760,40,60)	(38,2,3)	(1,2,3)
B2-GC1	Bump	0.5	2000	(760,40,60)	(38,2,3)	(1,2,3)
B2-GC2	Bump	0.5	5000	(760,40,60)	(38,2,3)	(1,2,3)

Figure 2: Schematic of the initial condition for turbidity currents interacting with a Gaussian-bump.
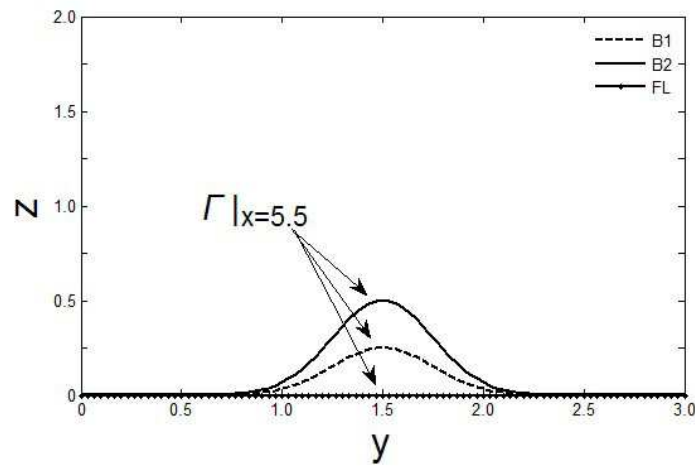

Figure 3: Three different heights of the Gaussian-bump at the bottom surface in simulations FL $(h=0)$, **B1** $(h=0.25)$ and **B2** $(h=0.5)$, respectively. In the streamwise direction, the highest point is located at $x=5.5$.

In this paper, the bump configuration on the bottom surface is defined as:

$$Z=\Gamma(x,y), \tag{3.1}$$

$$\Gamma(x,y)=h\exp\left(-\frac{(x-x_b)^2+(y-y_b)^2}{2\varepsilon^2}\right). \tag{3.2}$$

Here, (x_b,y_b) denotes the center of the Gaussian bump, which is $(5.5,1.5)$, and the width is set at $\varepsilon=0.25$. The bump height h is 0.25 for the **B1** case, and 0.5 for the **B2**, **B2−GC1** and **B2−GC2** cases (see Fig. 3). Note that the initial relative mass fraction held still by the lock is chosen to be 50% (i.e. $c_1=0.5$ and $c_2=0.5$) for all the cases under investigation.

3.2 Boundary conditions

3.2.1 Velocity boundary conditions

No-slip boundary conditions are applied on the bottom wall and on the left/right side walls. Free-slip boundary conditions are imposed on the top wall and up-stream/downstream side walls.

3.2.2 Concentration boundary conditions

As for the concentration field, the upstream, downstream, left and right boundary conditions are imposed as

$$
\begin{cases}
\frac{\partial c_i}{\partial x} = 0 & \text{at the upstream and downstream sides } (x=0,L_x), \\
\frac{\partial c_i}{\partial y} = 0 & \text{at left and right walls } (y=0,L_y).
\end{cases}
\tag{3.3}
$$

No-flux condition is specified at the top boundary to ensure that no particles are allowed to penetrate into this boundary [15]:

$$
c_i u_s^i + \frac{1}{Sc_i Re} \cdot \frac{\partial c_i}{\partial z} = 0 \quad \text{at top wall } (z=L_z).
\tag{3.4}
$$

At the bottom boundary, the suspended particles are assumed to leave the computational domain because of the settling velocity [15]. This is numerically equivalent to

$$
\frac{\partial c_i}{\partial t} = u_s^i \frac{\partial c_i}{\partial z} \quad \text{at bottom wall } (z=0).
\tag{3.5}
$$

4 Numerical method

4.1 Simulation of the concentration field

Resolving the discontinuous concentration field between the particle-laden water ($c=1$) and the clear water ($c=0$) is a critical issue in the current prediction. High-resolution advection schemes can be used to capture such a step-like function moving with the local flow velocity since numerical oscillations across the interface can be effectively suppressed [40, 41]. To reduce oscillatory and distorted solutions, the tangent of hyperbola for interface capturing (THINC) scheme can be employed as well to compute the numerical flux for the step-like function [42–44]. High-order schemes such as the compact difference (CD) and combined compact difference (CCD) schemes will inevitably produce numerical oscillations near discontinuities, thereby resulting in an incorrect prediction of the concentration. Section 4.1.1 and Section 4.1.2 are aimed to tackle this difficulty by applying the upwinding compact difference scheme.

4.1.1   Smoothen the initial discontinuous concentration field

A discontinuous concentration profile prescribed at the initial time $t=0$ generates most often spurious oscillations. To avoid generating any unphysical instability relevant to the Gibbs phenomenon, the sharp interface will be smeared over a few grid spacings by the introduced smoothed Heaviside function:

$$c(x,t=0)=\mathbf{H}(\phi), \tag{4.1}$$

where

$$\mathbf{H}(\phi)=\begin{cases} 0; & \text{if } \phi<-1.5\Delta x, \\ \frac{1}{2}[1+\frac{2\phi}{3\Delta x}+\frac{1}{\pi}\sin(\frac{2\pi\phi}{3\Delta x})]; & \text{if } |\phi|\leq1.5\Delta x, \\ 1; & \text{if } \phi>1.5\Delta x. \end{cases} \tag{4.2}$$

In Eq. (4.2), the function ϕ is the signed distance function and Δx is the grid spacing. The signed distance function in the particle-laden water and clear water is defined in a sense that the function ϕ_0 has the value of 1 in the particle-laden water and -1 in the clear water. The condition of $|\nabla\phi|=1$ is imposed to keep the discontinuous function ϕ_0 as a signed distance function. In other words, the following Hamilton-Jacobi equation will be chosen and solved [45–49]

$$\phi_\tau+\text{sgn}(\phi_0)(|\nabla\phi|-1)=0. \tag{4.3}$$

Note that the signed distance function ϕ is positive in the particle-laden water while is negative in the water after initializing the function ϕ_0. Fig. 4 shows the smoothing process on the initial discontinuous concentration field c. The fifth-order weighted essentially non-oscillatory (WENO5) scheme [47] and the third-order total variation diminishing Runge-Kutta (TVD-RK3) scheme [50] are applied together to approximate the spatial derivative term and the temporal derivative term, respectively, shown in the initialization equation (4.3). Application of Hamilton-Jacobi equation has successfully predicted the dam-break flow, Rayleigh-Taylor instability, and dislocation dynamics problems [48,49].

4.1.2   Approximation of the convection and diffusion terms in the concentration equation

After smoothing the discontinuous concentration field, the upwinding combined compact difference (UCCD) scheme developed for approximation of the spatial derivative term c_x is presented. The novelty of the currently employed combined compact difference scheme is that the derivative term c_{xx} is also considered as an unknown variable at each grid point in the derivation of the numerical scheme for c_x. The aim is to get the solution of a spectral-like resolution. In a four-point grid stencil, the numerical schemes
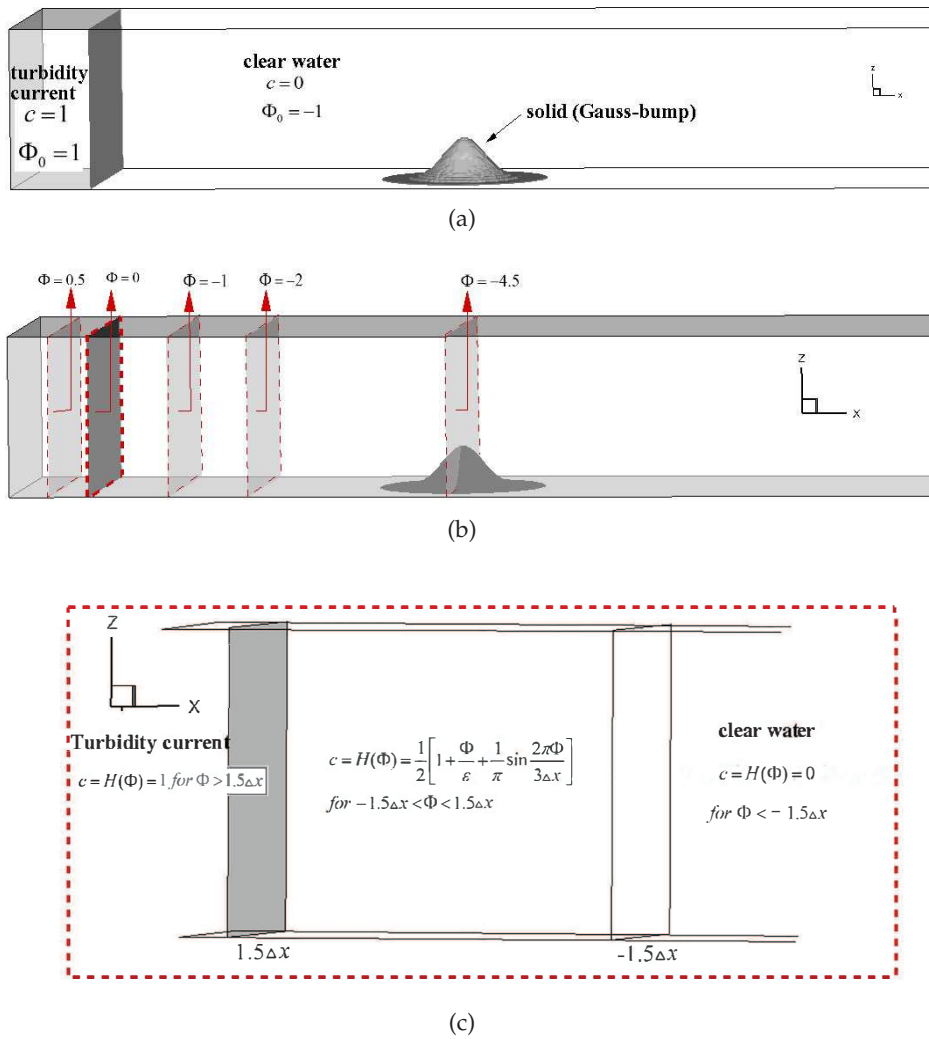
(a)

(b)

(c)

Figure 4: (a) Schematic of the initial concentration field of the particles and the color function ϕ_0; (b) Color function ϕ_0 has been initialized to sign distance function; (c) Substitution of ϕ into $H(\phi)$ to derive the continuous field c.

for $\frac{\partial c}{\partial x}$ and $\frac{\partial^2 c}{\partial x^2}$ are expressed below

$$\mathbf{a_1}\frac{\partial c}{\partial x}\Big|_{i-1} + \frac{\partial c}{\partial x}\Big|_i + \mathbf{a_3}\frac{\partial c}{\partial x}\Big|_{i+1}$$
$$= \frac{1}{h}(\mathbf{c_1}c_{i-2} + \mathbf{c_2}c_{i-1} + \mathbf{c_3}c_i) - h\left(\mathbf{b_1}\frac{\partial^2 c}{\partial x^2}\Big|_{i-1} + \mathbf{b_2}\frac{\partial^2 c}{\partial x^2}\Big|_i + \mathbf{b_3}\frac{\partial^2 c}{\partial x^2}\Big|_{i+1}\right), \quad (4.4)$$

$$-\frac{1}{8}\frac{\partial^2 c}{\partial x^2}\Big|_{i-1} + \frac{\partial^2 c}{\partial x^2}\Big|_i - \frac{1}{8}\frac{\partial^2 c}{\partial x^2}\Big|_{i+1}$$
$$= \frac{3}{h^2}(c_{i-1} - 2c_i + c_{i+1}) - \frac{9}{8h}\left(-\frac{\partial c}{\partial x}\Big|_{i-1} + \frac{\partial c}{\partial x}\Big|_{i+1}\right). \quad (4.5)$$

The coefficients shown in Eq. (4.5) are derived by virtue of the numerical method underlying the Taylor series expansion. The leading truncation error terms are eliminated by the modified equation analysis, thereby enabling us to get sixth-order accuracy [51]. After reducing the dispersion and dissipation errors by using the dispersion-relation-preserving scheme introduced in [25], the eight introduced unknown coefficients shown in Eq. (4.4) can be uniquely determined as $a_1 = 0.888252$, $a_3 = 0.049229$, $b_1 = 0.150072$, $b_2 = -0.250713$, $b_3 = -0.012416$, $c_1 = 0.016662$, $c_2 = -1.970805$ and $c_3 = 1.954143$. Application of this upwinding scheme developed in the stencil points $i-2$, $i-1$, i and $i+1$ for $\frac{\partial c}{\partial x}$ yields sixth-order spatial accuracy according to the following derived modified equation for $\frac{\partial c}{\partial x}$

$$\frac{\partial c}{\partial x} = \frac{\partial c}{\partial x}|_{exact} + 0.424003657 \times 10^{-6} \, h^6 \frac{\partial^7 c}{\partial x^7} + \text{High order terms.} \tag{4.6}$$

4.1.3 Time integration of the concentration equation

To integrate the concentration transport equation given below

$$\frac{dc_i}{dt} = L(c_i) = -[(u_i + u_s^i e^g) \cdot \nabla c_i] + \frac{1}{Sc_i Re} \nabla^2 c_i, \tag{4.7}$$

the third-order TVD Runge-Kutta (TVD-RK3) scheme is applied [50]. The solution of this ordinary differential equation is obtained through the following three solution steps

$$c_i^{(1)} = c_i^{(n)} + \Delta t L(c_i^{(n)}), \tag{4.8}$$

$$c_i^{(2)} = \frac{3}{4} c_i^{(n)} + \frac{1}{4} c_i^{(1)} + \frac{1}{4} \Delta t L(c_i^{(1)}), \tag{4.9}$$

$$c_i^{(n+1)} = \frac{1}{3} c_i^{(n)} + \frac{2}{3} c_i^{(2)} + \frac{2}{3} \Delta t L(c_i^{(2)}). \tag{4.10}$$

4.1.4 Solution procedures for the calculation of concentration equation

High-resolution schemes such as WENO and ENO surely can suppress numerical oscillations. Different from using high-resolution schemes, however, this solution algorithm aims to propose a compact difference scheme to suppress numerical oscillations. In all our cases, the error range of the total concentration in each Δt is 0.001%, when we filter the under-shoot/over-shoot values through **Step G**. The computational procedures employed to obtain the discontinuous concentration field solution by the upwinding combined compact difference (UCCD) scheme are summarized as below:

(**Step A**) Prescribe the values of $\phi_0 = 1$ in the particle-laden water and $\phi_0 = -1$ in the clear water, respectively.

(**Step B**) Calculate the initialization equation (i.e. Eq. (4.3)) to obtain the signed distance function ϕ at time $t = \mathbf{L}$, where $\mathbf{L}$ is set to be the maximum length of the computational domain.

(**Step C**) Define the concentration field variable c according to the signed distance function ϕ shown in Eq. (4.1).

(**Step D**) Set $c_1 = \frac{c}{2}$ and $c_2 = \frac{c}{2}$.

(**Step E**) Approximate the convection and diffusion terms in Eq. (2.5) using the proposed UCCD scheme described in Section 4.1.2.

(**Step F**) Approximate the temporal derivative term using the third-order TVD Runge-Kutta scheme described in Section 4.1.3.

(**Step G**) If $c_i > 0.5$, set $c_i = 0.5$; if $c_i < 0$, set $c_i = 0$ for i=1,2.

(**Step H**) Repeat the steps from step "**E**" to step "**G**" within each time loop. Note that the procedure (i.e. "**Step A**" to "**Step C**") taken to smooth the discontinuous concentration field is performed only once at $t=0$.

4.2 Incompressible Navier-Stokes solution solver

4.2.1 Approximation of the convection and diffusion terms in the momentum equations

The convection terms in the momentum equations are discretized using the third-order Quadratic Upstream Interpolation for Convective Kinematics (QUICK) scheme. Take $u\frac{\partial u}{\partial x}$ as an example, this term can be approximated as

$$u\frac{\partial u}{\partial x} = \frac{u}{2\triangle x}\left(u_{i+1,j,k} - u_{i-1,j,k}\right) - \frac{u^+ \, \mathcal{CF}}{\triangle x}\left(u_{i+1,j,k} - 3u_{i+1,j,k} + 3u_{i-1,j,k} - u_{i-2,j,k}\right)$$
$$- \frac{u^- \, \mathcal{CF}}{\triangle x}\left(u_{i+2,j,k} - 3u_{i+1,j,k} + u_{i,j,k} - u_{i-1,j,k}\right), \tag{4.11}$$

where $u^+ = \frac{1}{2}(u_{i,j,k} + |u_{i,j,k}|)$, $u^- = \frac{1}{2}(u_{i,j,k} - |u_{i,j,k}|)$ and $\mathcal{CF} = 0.125$. Note that the choice of $\mathcal{CF} = 0$, $\mathcal{CF} = 0.25$ and $\mathcal{CF} = 0.5$ corresponds to the center difference method, second-order upwind scheme and the Fromm's scheme, respectively, based on the curvature-factor convection scheme of Minkowcyz and Sparrow [52]. The viscous terms in the x-momentum equation can be approximated by the second-order accurate center difference scheme given below

$$\frac{\partial^2 u}{\partial \mathbf{x}^2} = \frac{u_{i+1,j,k} - 2u_{i,j,k} + u_{i-1,j,k}}{\triangle \mathbf{x}^2}. \tag{4.12}$$

4.3 Pressure field

For the sake of effectively solving the pressure field, the projection method introduced by Chorin in 1972 [53] applied together with the use of IB method has been employed to solve the time-dependent incompressible flow solutions. In Eq. (2.2), the time derivative

term is approximated in a way given below to obtain the intermediate velocity $\mathbf{u}^*$ without considering the pressure and the virtual force terms

$$\frac{\mathbf{u}^*-\mathbf{u}^n}{\triangle t}+\mathbf{u}\cdot\nabla\mathbf{u}=\frac{1}{Re}\nabla^2\mathbf{u}+c\,\mathbf{e_g}. \tag{4.13}$$

By taking the divergence operator on Eq. (4.13) and imposing the constraint condition $\nabla\cdot\mathbf{u}'=0$, the Poisson equation for p^{n+1} can be derived as

$$\nabla^2 p^{n+1}=\frac{1}{\Delta t}\nabla\mathbf{u}^*. \tag{4.14}$$

Eq. (4.14) is then solved using the Gauss-Seidel iterative solver to get the solution of p^{n+1}. The solutions $\mathbf{u}'$ are computed from the following equations, respectively

$$\frac{\mathbf{u}'-\mathbf{u}^*}{\triangle t}+\frac{\partial p^{n+1}}{\partial\mathbf{x}}=0. \tag{4.15}$$

After obtaining the values of $\mathbf{u}'$, the relation between $\mathbf{u}^{n+1}$ and the virtual force $\mathbf{f}$ can be shown as

$$\frac{\mathbf{u}^{n+1}-\mathbf{u}'}{\triangle t}=\eta\,\mathbf{f}^{n+1}, \tag{4.16}$$

where η is the percentage of the solid volume in one cell. Therefore, the force $\mathbf{f}^{n+1}$ can be calculated according to the following equations to account for the presence of solid bumps

$$\begin{cases} \eta=0,\ \mathbf{u}^{n+1}=\mathbf{u}',\ \mathbf{f}^{n+1}=0 & \text{on fluid,} \\ \eta\neq 0,\ \mathbf{u}^{n+1}=\mathbf{u}_{solid},\ \mathbf{f}^{n+1}=\frac{\mathbf{u}_{solid}-\mathbf{u}'}{\eta\triangle t} & \text{on solid.} \end{cases} \tag{4.17}$$

In Eq. (4.17), $\mathbf{u}_{solid}$ is the solid velocity vector. We provide a detailed calculation for volume fraction of a solid (i.e. η) in Appendix.

5 Validation studies

Ref. [15] presents a gravity current problem where the suspended mass of particle is calculated. The model is validated using this problem. Sensitivity of the computational grids is assessed by calculating the suspended mass of the gravity currents problem [15]:

$$m_s^i=\int_\Omega c_i\,dv,\quad i=1,2, \tag{5.1}$$

where Ω is the computational domain.

5.1　Grid sensitivity analysis

Fig. 5 presents the suspended particle mass against the temporal evolution obtained in 150×20, 375×50, 750×100 and 1125×150 grids. It is observed that results of the suspended particle mass for 375×50 and 750×100 grids are almost identical. In addition, the suspended particle mass matches quite well with the numerical result in [15]. After ensuring that the grids are independent of suspended particle mass, the grid interval (i.e. $\Delta x\!=\!0.05$) will be carried out in the following three-dimensional current simulations.
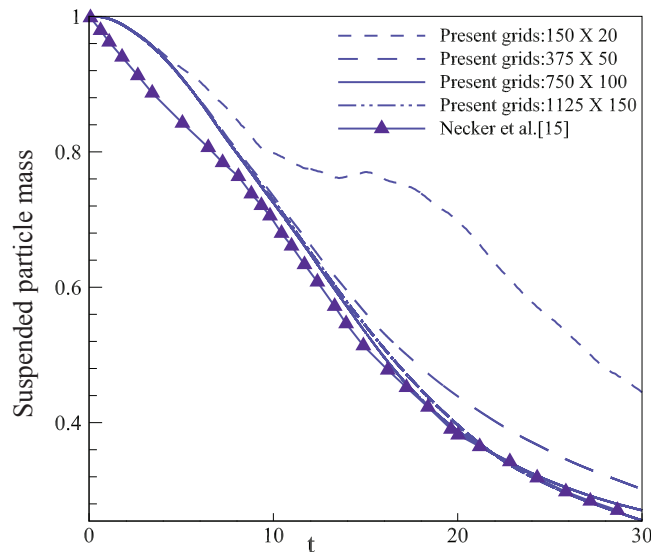
Figure 5: Grid sensitivity test for suspended particle mass.

5.2　Influence of smoothing procedure

The smoothing procedure introduced in Section 4.1.1 implies that the Heaviside function introduces an interface thickness which depends on the mesh size, and generates the discrepancy in suspend particle mass among different works. Therefore, the quantity of suspended particle mass is evaluated with/without smoothing procedure to investigate the performance of the present model. As is shown in Fig. 6, a numerical model with smoothing procedure tends to yield more accurate results of the concentration field than a numerical model without smoothing procedure. It is found that Fig. 6(b) exhibits unreasonable contours of the concentration field (i.e. $c\!>\!1$ at some nodal points).

5.3　Influence of filter/no filter

The present results will never exceed 1 in the sense that we have already filtered the concentration through Step G. In fact, the upwinding combined compact difference

(a)

(b)
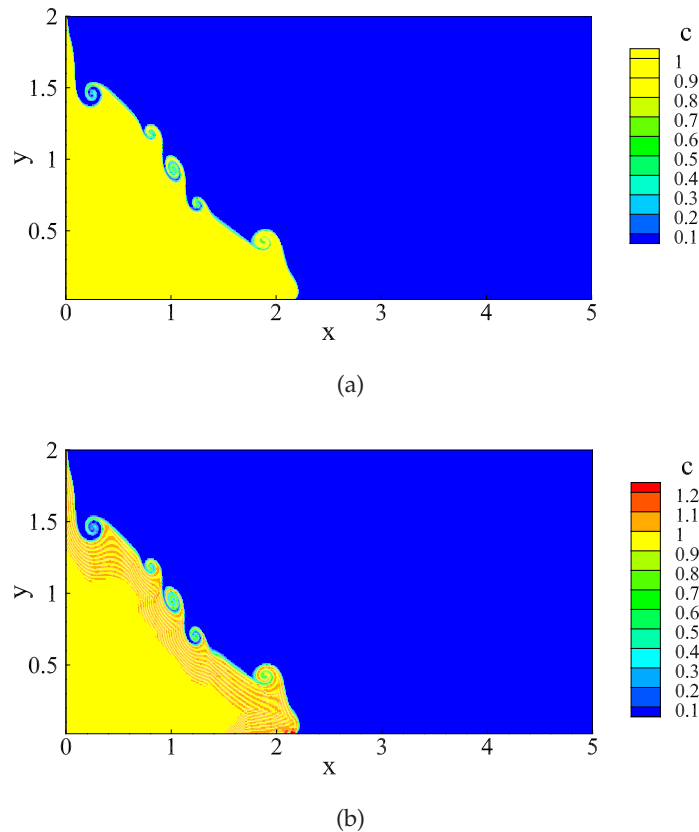
Figure 6: Influence of the smoothing procedure for concentration values at $t = 0.7$. (a) With smoothing procedure; (b) Without smoothing procedure.

(UCCD) scheme described in Section 4.1.2 is not a non-oscillatory one, so that the under-shoot/over-shoot values for concentration field occur inevitably. We compare the filtered results with the non-filtered ones for 375×50 girds solution. In Fig. 7, one can see that under-shoot/over-shoot values appear inevitably in the concentration profile when the non-filtered step is not used.

5.4 Comparison of upwind scheme and high resolution scheme

Approximation of the convective terms in the concentration equation requires taking the upwind nodal solutions along the flow direction into consideration. To show the advantage of the present UCCD scheme, we compared the numerical results derived from using the weighted essentially non-oscillatory scheme [47], QUICK scheme described in Section 4.2.1 and the proposed scheme for solving the first derivative terms in Eq. (2.5). For the sake of comparison, the numerical results by WENO, QUICK and the present

(a)

(b)
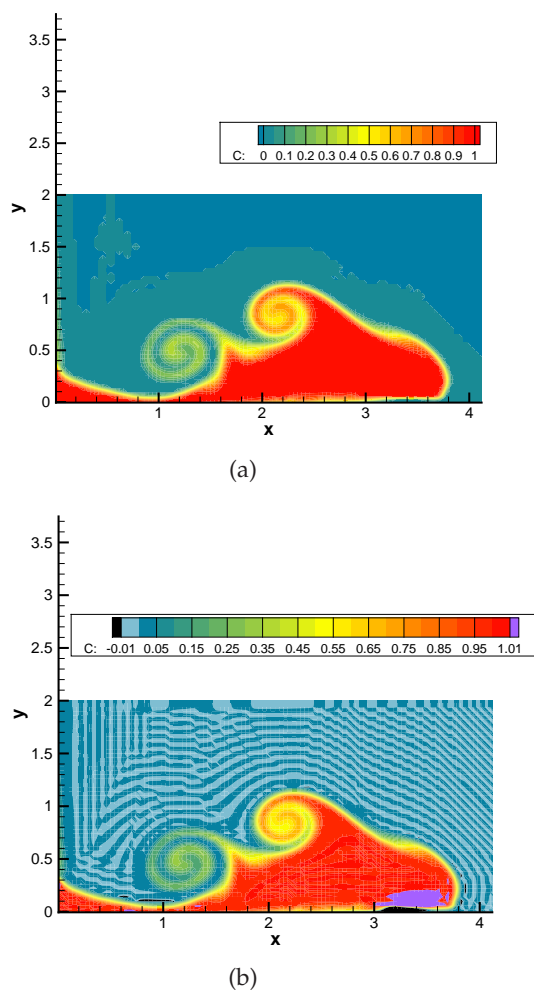
Figure 7: Influence of the filter for concentration values at $t=4.8$. (a) With filter; (b) Without filter.

method are plotted in Fig. 8(a)-(c). The numerical results with the 375×50 grid only present slight differences. Fig. 9 shows the comparison of the suspended mass using the above three schemes.

5.5 Effect of Schmidt numbers

The effect of the Schmidt number Sc_i on the dynamics of fluid flow is negligible when $Sc_i \geq \mathcal{O}(1)$. The value of Schmidt number is therefore set to unity [6]. In this study, different Schmidt numbers $Sc=1,20,100$ and $Sc=1000$ are adopted to investigate whether Schmidt number affects the suspended particle mass. In Fig. 10, one can see that the suspended particle mass can be accurately predicted at different Schmidt numbers.
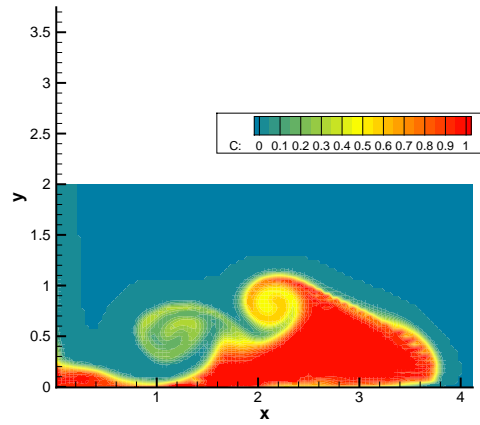
(a)
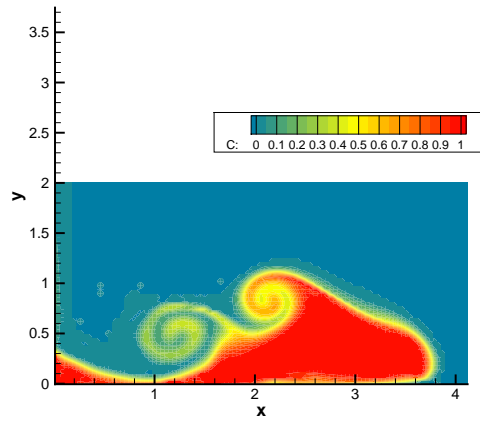
(b)
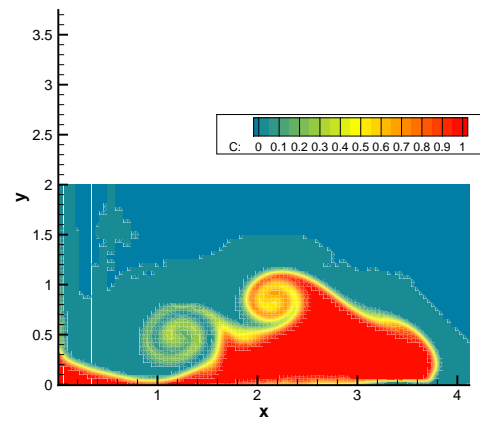
(c)

Figure 8: Comparison with difference scheme for concentration values at $t=4.8$. (a) WENO scheme; (b) QUICK scheme; (c) Present scheme.
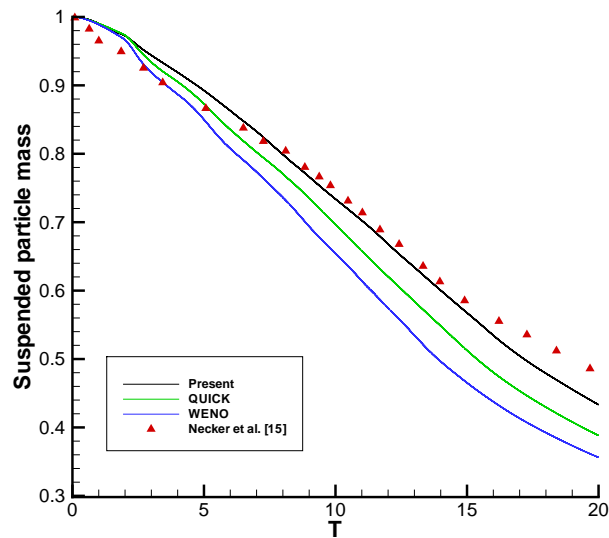
Figure 9: Comparison of upwinding scheme and high resolution scheme for suspended particle mass.
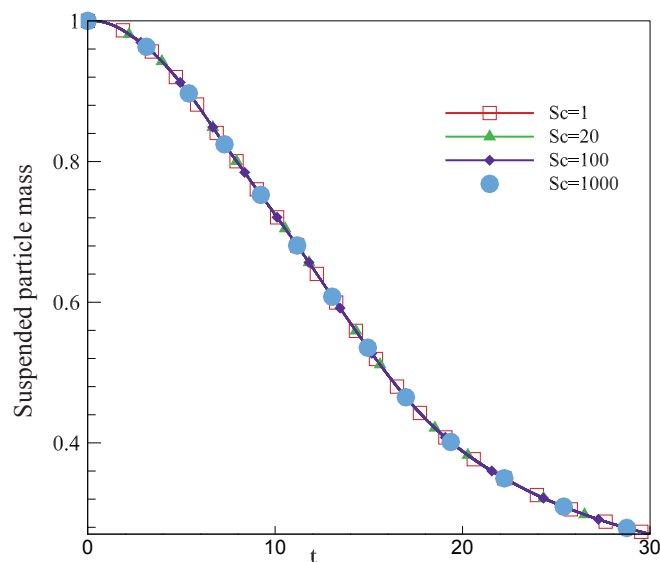
Figure 10: Effect of Schmidt number on suspended particle mass.

Bonometti and Balanchandar [54] pointed out that effect of the Schmidt number on the concentration field depends on the Reynolds number. Therefore, the results of four cases with $Re = 100$, 1000, 5000 and 10000 at time $t = 8$ are selected to see whether the smoothing procedure and artificial dissipation provided for the upwind scheme hide these differences. Fig. 11(a) presents the results of $Re = 100$. The left column shows the results using QUICK and WENO schemes without smoothing, and the right column shows
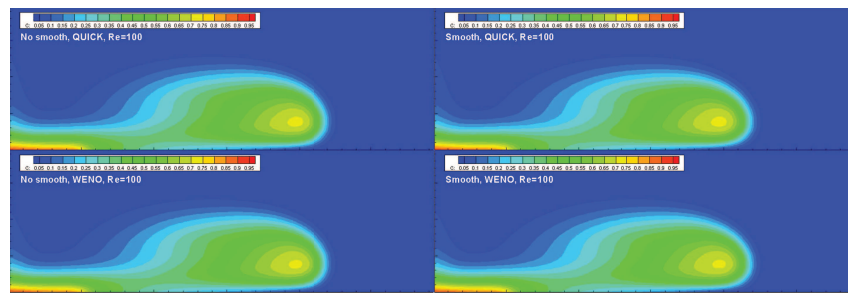
(a)
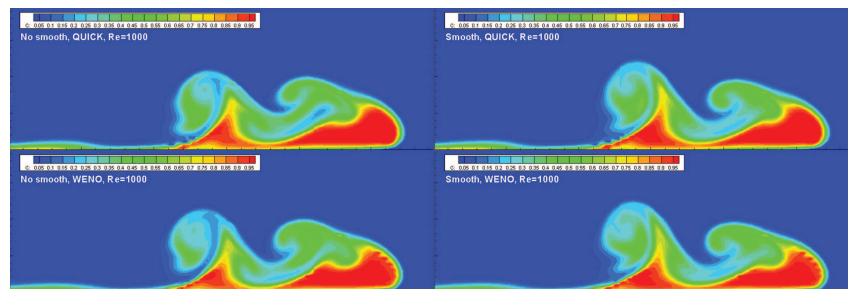
(b)
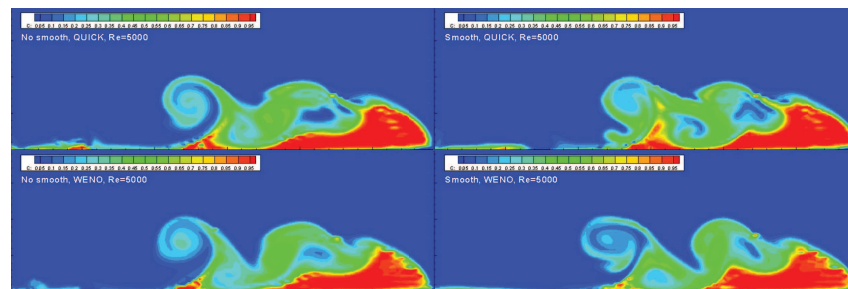
(c)
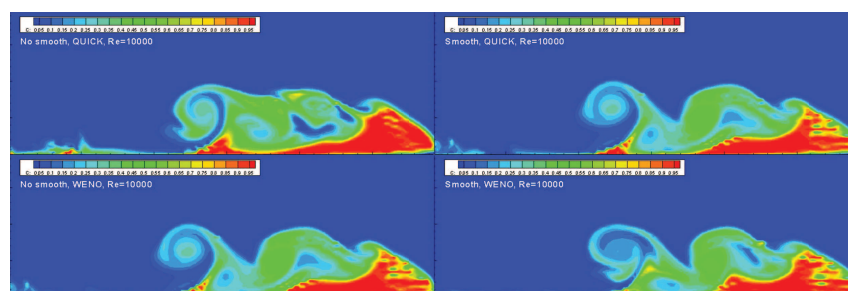
(d)

Figure 11: Comparison of with/without smooth procedure and WENO/QUICK scheme for concentration values at $t=8.0$ at four distinct Reynolds number. (a) Re$=100$; (b) Re$=1000$; (c) Re$=5000$; (d) Re$=10000$.

the results with smoothing. It can be seen from the four subfigures that the structure of the mixing region and the front velocities are almost the same. The $Re=1000$ results are shown in Fig. 11(b). Slight differences can be found in the mixing region structure using both schemes, both with and without smoothing, implying the slight influence of artificial dissipation provided by upwind schemes on the mixing region structure. However, neither the smoothing procedure nor the artificial dissipation affects the front velocity. In Fig. 11(c) with $Re=5000$, the front velocity is not influenced by smoothing procedure or artificial dissipation either. In Fig. 11(d) with $Re=10000$, great disparities can be found in the mixing region structure between the two schemes, both with and without smoothing. This indicates that artificial dissipation can influence the structure of the mixing region. However, the front velocity is not influenced.

## 6   Current properties and energy budget

The simulated current properties, including the front location, suspended mass, sedimentation rate and energy budget, will be compared with the numerical results of Nasr-Azadani and Meiburg [7]. The predicted time-evolving structures of the turbidity current and gravity current are plotted in Fig. 12 and Fig. 13 for the cases **B1** and **B2**−**GC1**. A uniform Cartesian grid with the spacing of 0.05 in all the three directions is employed. The time interval Δt is equal to $0.005\Delta x$, which is 0.00025.

6.1   Front location

The front location is defined as the farthest downstream location, at which c_f exceeds the threshold value of 10^{-3} [7]. In Fig. 14, the predicted front locations are seen to match well with the numerical results of Nasr-Azadani and Meiburg [7] for the turbidity current cases **B1** and **B2** simulated at $Re=2000$. Fig. 14 also shows that the present results for the gravity current case (i.e. **B2**−**GC1** and **B2**−**GC2**) and the numerical results of Nasr-Azadani and Meiburg [7] match very well at $Re=2000$ and $Re=5000$. The Reynolds number seems to have a negligible effect on the front velocity. In [55, 56], details of the turbidity current propagation in three stages are shown. In the first stage (or slumping stage), in which the lock-exchange sediment propagates at a constant velocity, the effect of the settling velocity on the front velocity of the turbidity current can be almost ignored. It means that the front velocity of the current is nearly independent of the settling velocity in the slumping stage. Fig. 14 shows that turbidity currents in the slumping stage propagate at the constant velocity before $t=15$. This simulated result is consistent with those in [55, 56]. In Fig. 15, the front velocity for the turbidity current (Case **B2**) and the gravity current (Case **B2**−**GC1**) are similar to each other when the current arrives at the bump. Afterwards, the settled sediment particles cause the reduction of front velocity to occur for the turbidity current. However, the current head for the gravity current is still thick and it moves faster.
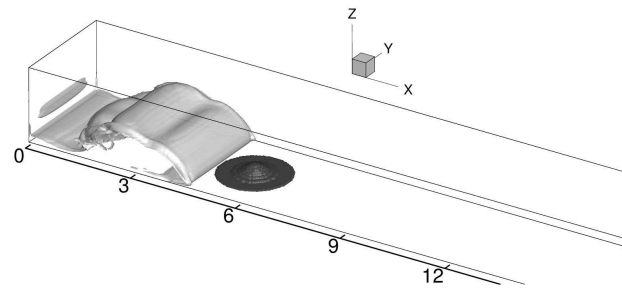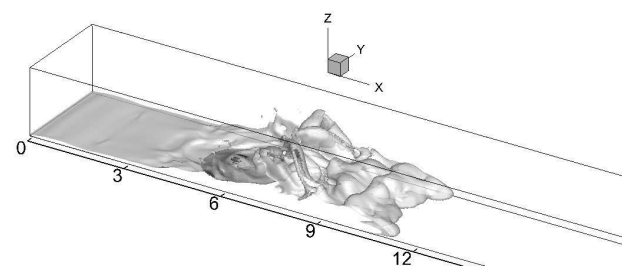
(a)
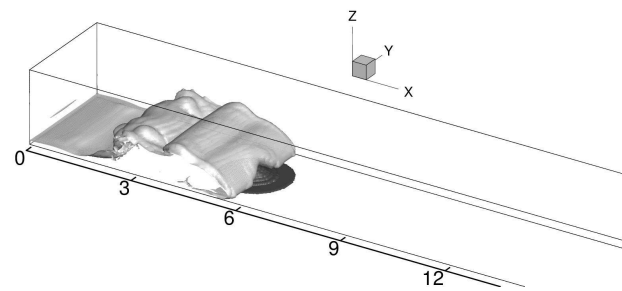
(b)
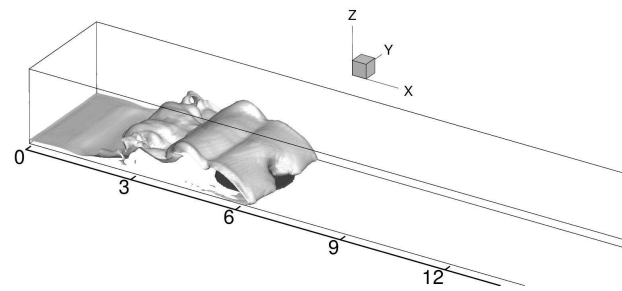
(c)

(d)

Figure 12: Time evolution of the turbidity currents over the Gaussian-bump at $t = 6$, 8, 9, and 20. Iso-surfaces of the concentration field represent the $c = 0.1$ contour.
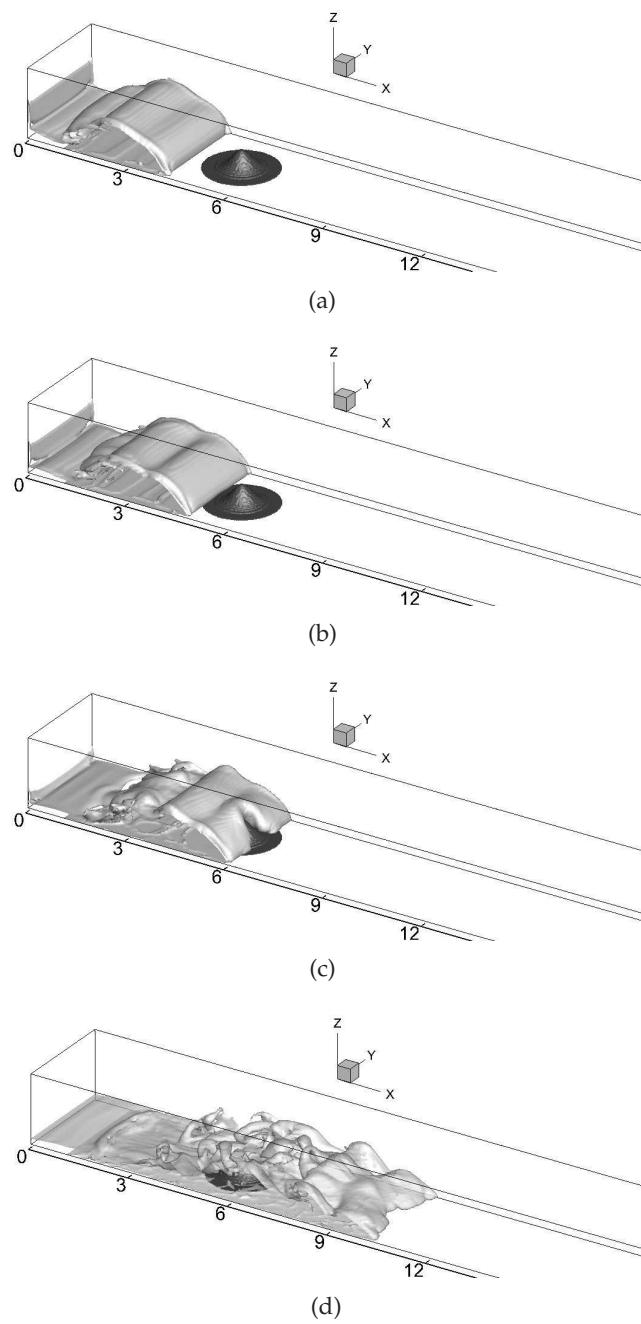
(a)

(b)

(c)

(d)

Figure 13: Time evolution of the compositional gravity currents over the Gaussian-bump at $t = 6$, 7, 9, and 14. Iso-surfaces of the concentration field represent the $c = 0.1$ contour.
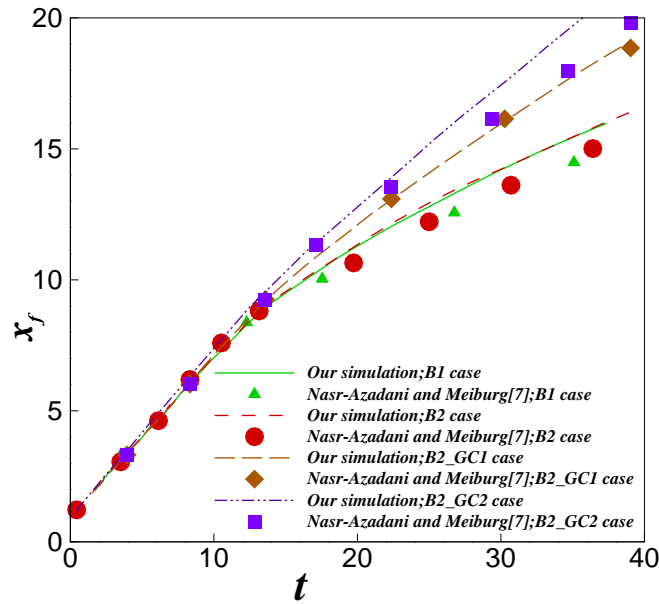
Figure 14: Comparison of the front locations $x_f(x)$ with the numerical result of Nasr-Azadani and Meiburg [7].

6.2 Suspended mass

The suspended mass is defined in Eq. (5.1). Beyond $t=15$, turbidity currents gradually slow down (i.e. **B1**, **B2** cases) in comparison with the compositional gravity currents (i.e. **B2−GC1**,**B2−GC2** cases) as shown in Fig. 14 and Fig. 16. This predicted propagation is due to the decreased driving force as a result of the loss of suspended particles in turbidity. In Figs. 16(a) and 16(b), about 50% of the particle mass is still in suspension at $t=20$ for all the cases under investigation. It is implied that the presence of obstacles does not cast any significant influence on the mass of suspended particles.

The temporal evolution of turbidity current **B1** for coarse and fine particles are clearly exhibited in Fig. 17. During the early stage, the concentration field of coarse and fine particles are almost identical. By $t=16$, plenty of coarse particles have already been settled down, whereas most of fine particles are still in suspension. For the $Re=5000$ case (i.e. **B2−GC2** case) presented in Fig. 18, a significant effect of the Reynolds number on the flow evolution is revealed.

6.3 The sedimentation rate

On the bottom surface, the sedimentation rate, which is defined below as the time derivative of the suspended sediment mass, evolves with time

$$m_d^i = -\int_A u_s^i c_w^i \mathbf{e^g} \cdot \mathbf{n}\, d\mathbf{A}, \quad i=1,2. \tag{6.1}$$
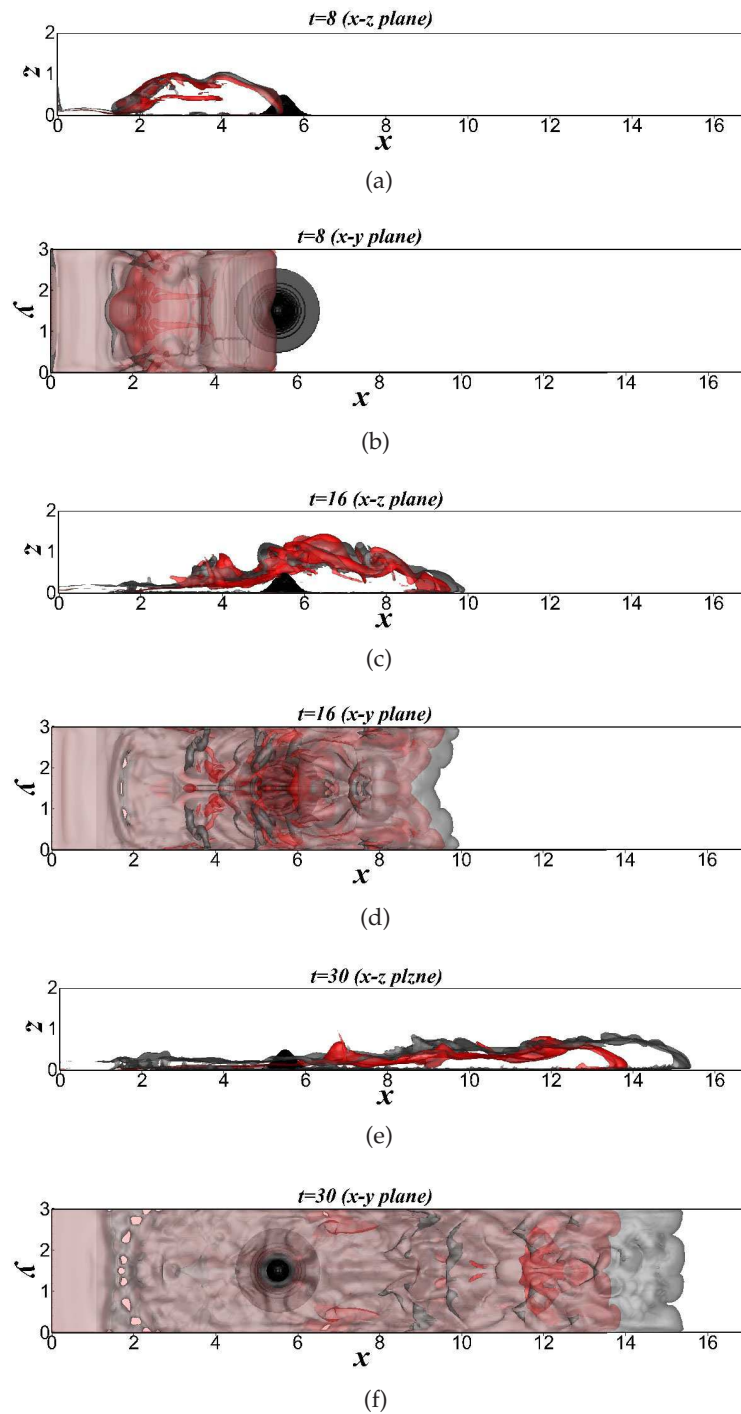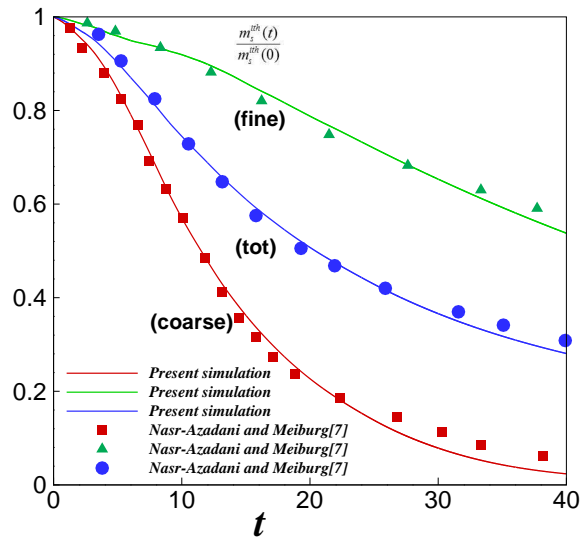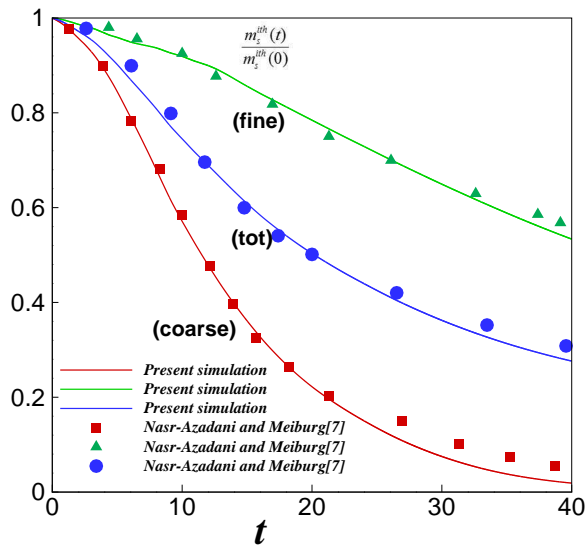
(a)

(b)

(c)

(d)

(e)

(f)

Figure 15: Front location for **B2** (the iso-surface in red) and **B2−GC1** (the iso-surface in gravy) cases and the bird's-eye view. (a),(b) $t=8$; (c),(d) $t=16$; (e),(f) $t=30$.

(a)

(b)

Figure 16: Suspended particle mass plotted as a function of time is compared with the numerical results of Nasr-Azadani and Meiburg [7]. Note that **coarse**, **fine** and **tot** in the figure refer to the normalized suspended masses of coarse $(u_s^1 = 0.03)$, fine $(u_s^2 = 0.006)$ and all particles, respectively. (a) **B1** case; (b) **B2** case.

In Eq. (6.1), **A** denotes the bottom surface area. In addition, **n** is the normal direction along the bottom surface of Gaussian-bump, and c_w^i represents the particle concentration at the bottom surface. Sedimentation rate against time for two turbidity cases **B1** and **B2**
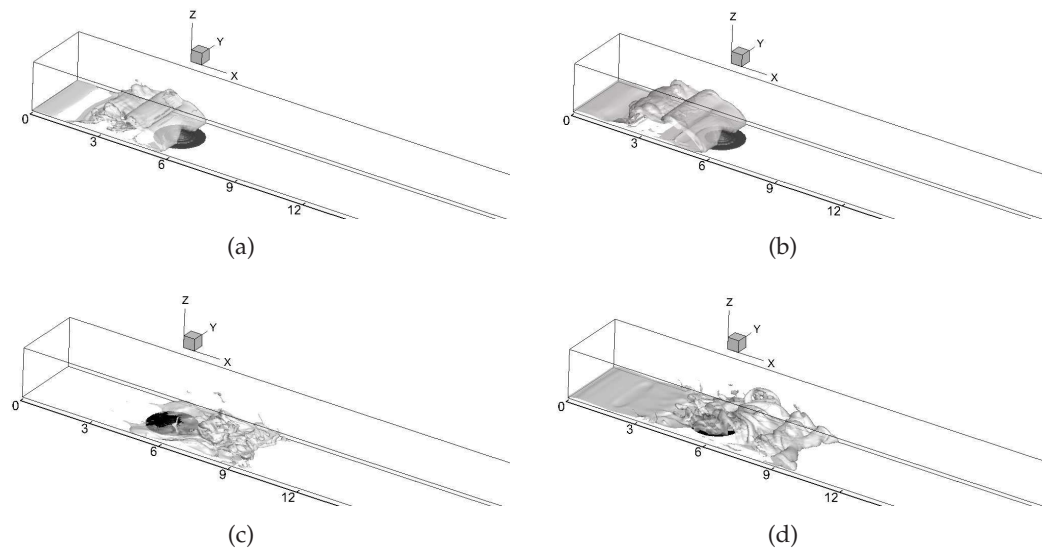
Figure 17: Iso-surfaces ($c=0.1$) of the concentration field are represented at $t=8$ and $t=16$ from top to bottom. (a),(c) coarse particles; (b),(d) fine particles.
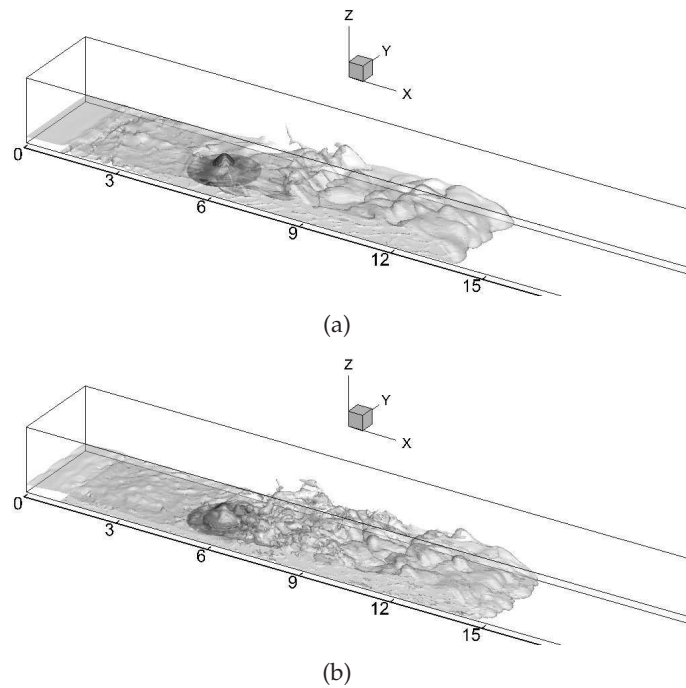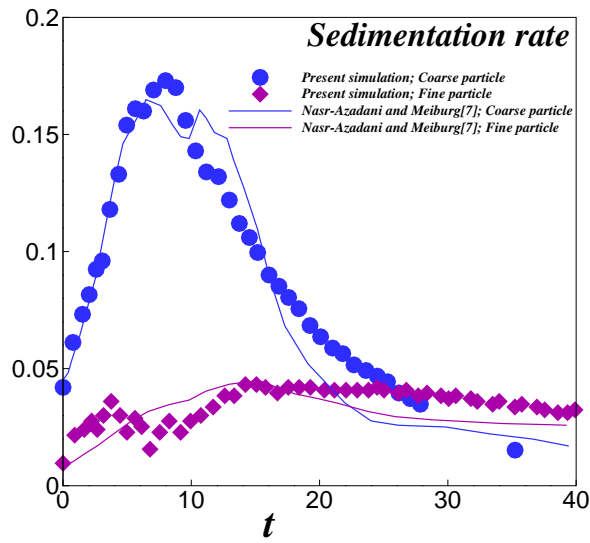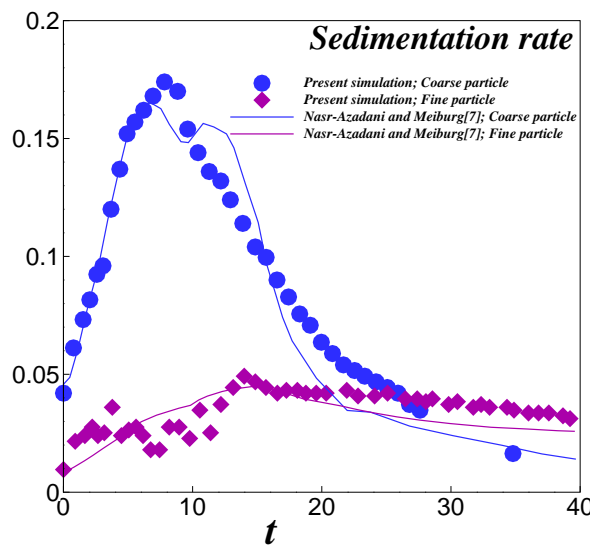

Figure 18: Time evolution of the turbidity currents over the bump at $t=25$. Iso-surfaces of the concentration field represent the $c_t=0.1$ contour. (a) for the **B2−GC1** case; (b) for the **B2−GC2** case.

(a)

(b)

Figure 19: Sedimentation rate plotted as the function of time for two turbidity cases are compared with the numerical results of Nasr-Azadani and Meiburg [7]. (a) **B1** case; (b) **B2** case.

.

are plotted in Fig. 19. Good agreement with the numerical results of Nasr-Azadani and Meiburg [7] can be seen. The sedimentation rate for both particle sizes show a dramatic change as the authors pointed out in [7,15]. The bottom topography only poses a weak impact on the sedimentation rate. In Fig. 20, the time evolution of the concentration
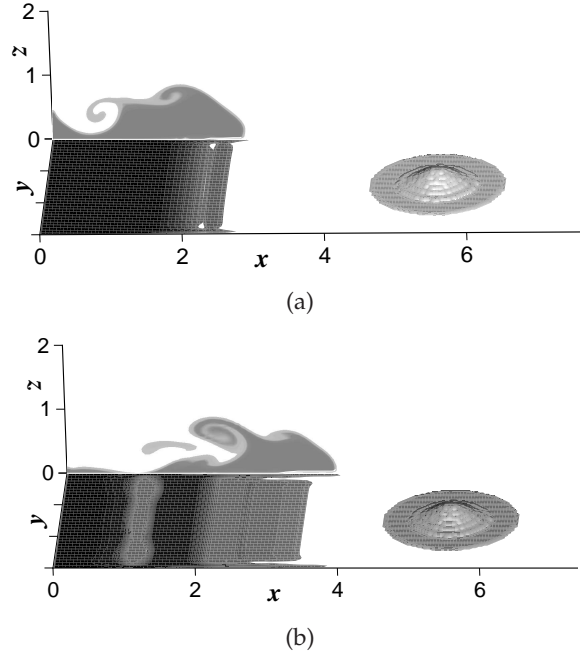
Figure 20: The concentration field c is predicted for case **B1**. (a) $t=4$; (b) $t=6$. Note that the vertical plane describes the particle concentration profile at $y=1.5$.

$c=0.95$ is exhibited. Since no-slip boundary condition is applied at the bottom wall, the particle concentration has been reduced.

6.4 Energy budget

The reduction of the mechanical energy is linked to three mechanisms that are responsible for the changes of ε_d (implying the loss due to viscous dissipation at macroscopic scale), ε_s (implying the loss due to viscous effect in the microscopic Stokes flow around each particle), ε_l (implying the deposition of particles along the bottom boundary)

$$\varepsilon_d = \int_\Omega \frac{2}{Re} S_{mn} S_{mn} \, dv, \quad S_{mn} = \frac{1}{2} \left(\frac{\partial u_m}{\partial x_n} + \frac{\partial u_n}{\partial x_m} \right), \tag{6.2}$$

$$\varepsilon_s = \sum_{i=1}^{2} \left(\int_\Omega u_s^i c_i dv \right), \tag{6.3}$$

$$\varepsilon_l = -\sum_{i=1}^{2} \left(\int_A z_\Gamma u_s^i c_w^i \mathbf{e_g} \cdot \mathbf{n} dA \right). \tag{6.4}$$

In Eq. (6.2), S_{mn} denotes the symmetric components in the velocity gradient tensor and z_Γ is the surface height along the bottom wall. The energy equation for the rate of change
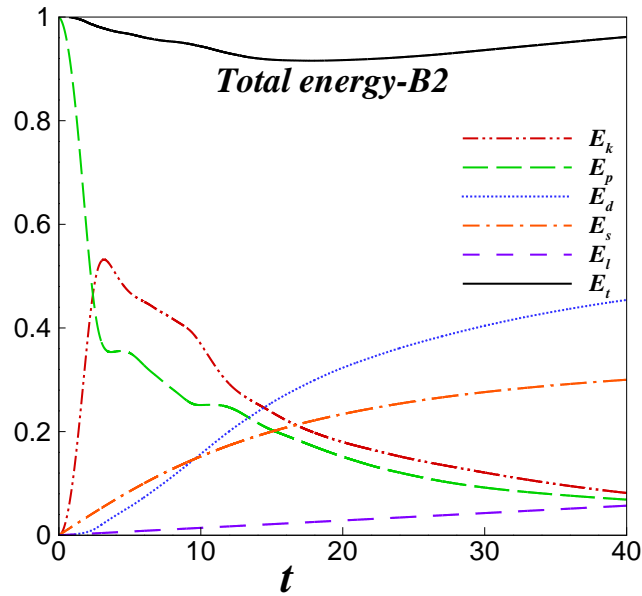
Figure 21: Time history of the predicted kinetic E_k, potential energy E_p, dissipation components E_d and E_s, the energy loss E_l due to particle settling on the bump for the **B2** case and E_t indicates the total energy. It is noted that all energy components have been normalized by the initial energy.

of the total mechanical energy is governed by

$$\frac{d}{dt}(E_k + E_p) = \varepsilon_d + \varepsilon_s + \varepsilon_l. \tag{6.5}$$

Here, E_k and E_p are the kinetic and potential energy components, respectively. Integration of Eq.(6.5) with respect to time leads to

$$E_k + E_p + E_d + E_s + E_l = const = E_{p0} + E_{k0} = E_t, \tag{6.6}$$

where

$$E_d(t) = \int_0^t \varepsilon_d(t)dt, \tag{6.7}$$

$$E_s(t) = \int_0^t \varepsilon_s(t)dt, \tag{6.8}$$

$$E_l(t) = \int_0^t \varepsilon_l(t)dt. \tag{6.9}$$

In Eq. (6.6), E_{p0} and E_{k0} represent the initial potential and kinetic energy in the domain. Note that the influence of the particle diffusion on the potential energy as indicated in [7] has been neglected. The predicted kinetic and potential energy results are compared with those of Nasr-Azadani and Meiburg [7] in Figs. 21-24 for the cases of **B1**, **B2** and
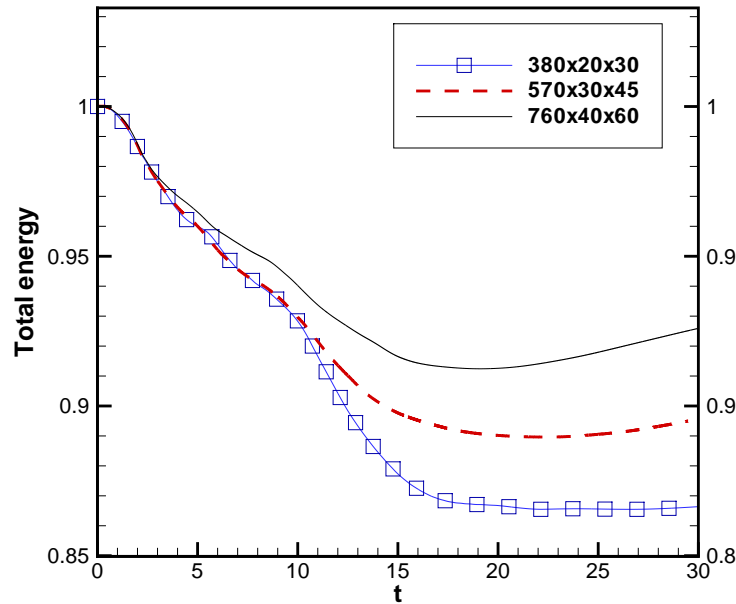
Figure 22: Total energy time series for three grids. Note that total energy has been normalized by the initial total energy.

B2−GC1. Fig. 21 illustrates the time history of all energy components for case **B2**. When the dense fluid is released, potential energy is rapidly converted to kinetic energy, which has reached its peak magnitude at $t \approx 5$. Since then, both the potential and kinetic energy components decline as a result of the viscous dissipation effect. As a result of the fact that the bump takes only a small fraction of the bottom boundary, particles settling on the bump (E_l) are of $\mathcal{O}(5\%)$. We have noticed that the total energy is not conserved in Fig. 21. We believe that this is caused by numerical errors, i.e., numerical dissipation and dispersion. In order to best conserve the energy, we calculated the results till time $t = 30$ in three grids, $380 \times 20 \times 30$, $570 \times 30 \times 45$ and $760 \times 40 \times 60$. As Fig. 22 shown, total energy loss for the coarsest grid is 13.5%, while that for the finest one is only 7.5%.

The kinetic and potential energy for **B1** and **B2** cases are compared in Fig. 23. The temporal evolution of the energy components for case **B2** resembles closely to that of case **B2−GC1** until $t = 4$ (Figs. 23(c) and 23(d)). In Fig. 24, the viscous (E_d) and Stokes (E_s) dissipation components are compared with the numerical results of Nasr-Azadani and Meiburg [7]. It is noted that E_s is present only in the turbidity currents **B1** and **B2** since the settling velocity is not taken into account.

7 Concluding remarks

In this paper the upwinding combined compact difference scheme is applied together with the immersed boundary method in collocated grids to predict gravity and turbidity
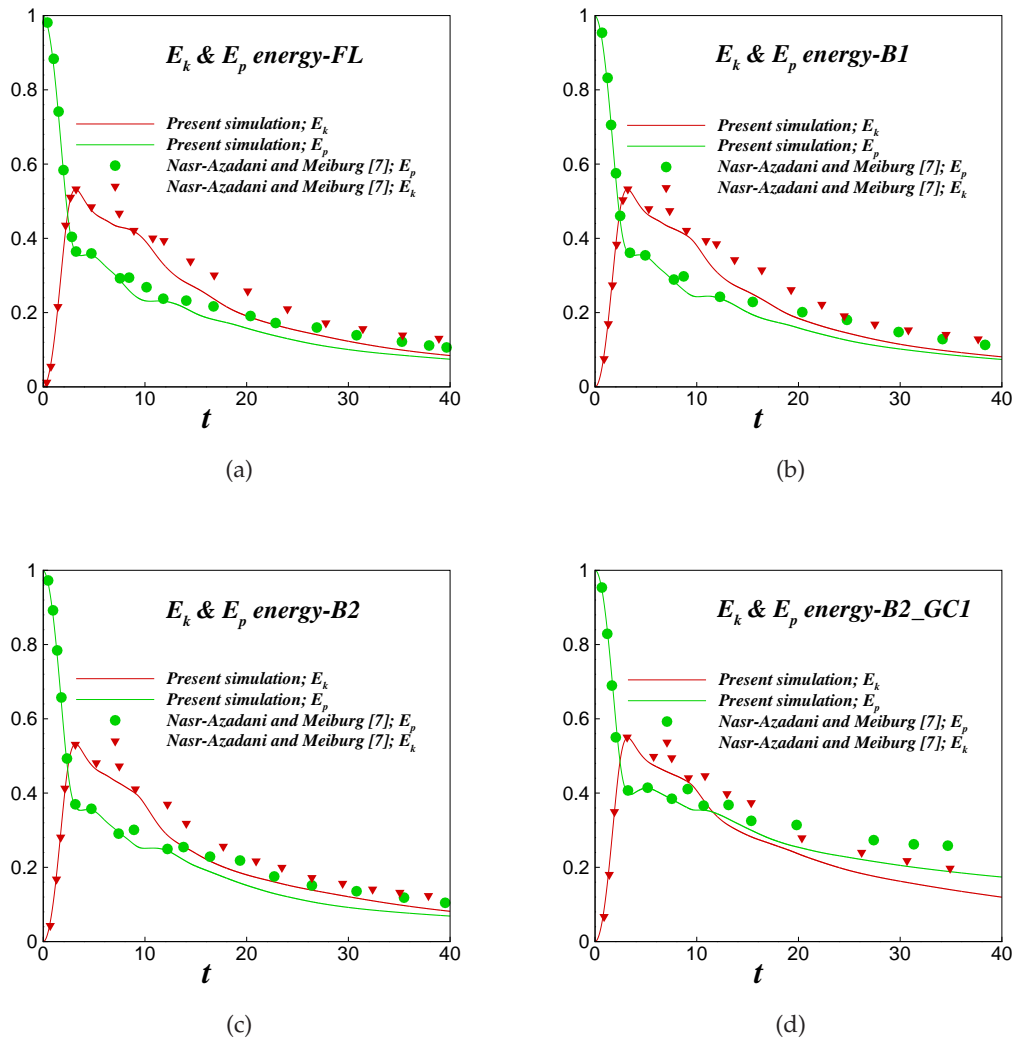
Figure 23: Time history of the predicted kinetic and potential energies, which are compared with the numerical results of Nasr-Azadani and Meiburg [7]. (a) **FL**; (b) **B1**; (c) **B2**; (d) **B2−CG1**.

current flows, inside which there is a solid Gaussian-bump. The discontinuous concentration field has been calculated by the proposed algorithm described in Section 4.1 to avoid numerical oscillations near discontinuities. In other words, this algorithm smooths the discontinuous initial concentration field by solving the Hamilton-Jacobi equation and then approximates the smoothed concentration field by solving the concentration transport equation using the UCCD scheme. IB method has been applied aiming to easily and accurately predict fluid flows in a domain with complex geometry. This new model developed underlying the projection method can be successfully applied to compute the
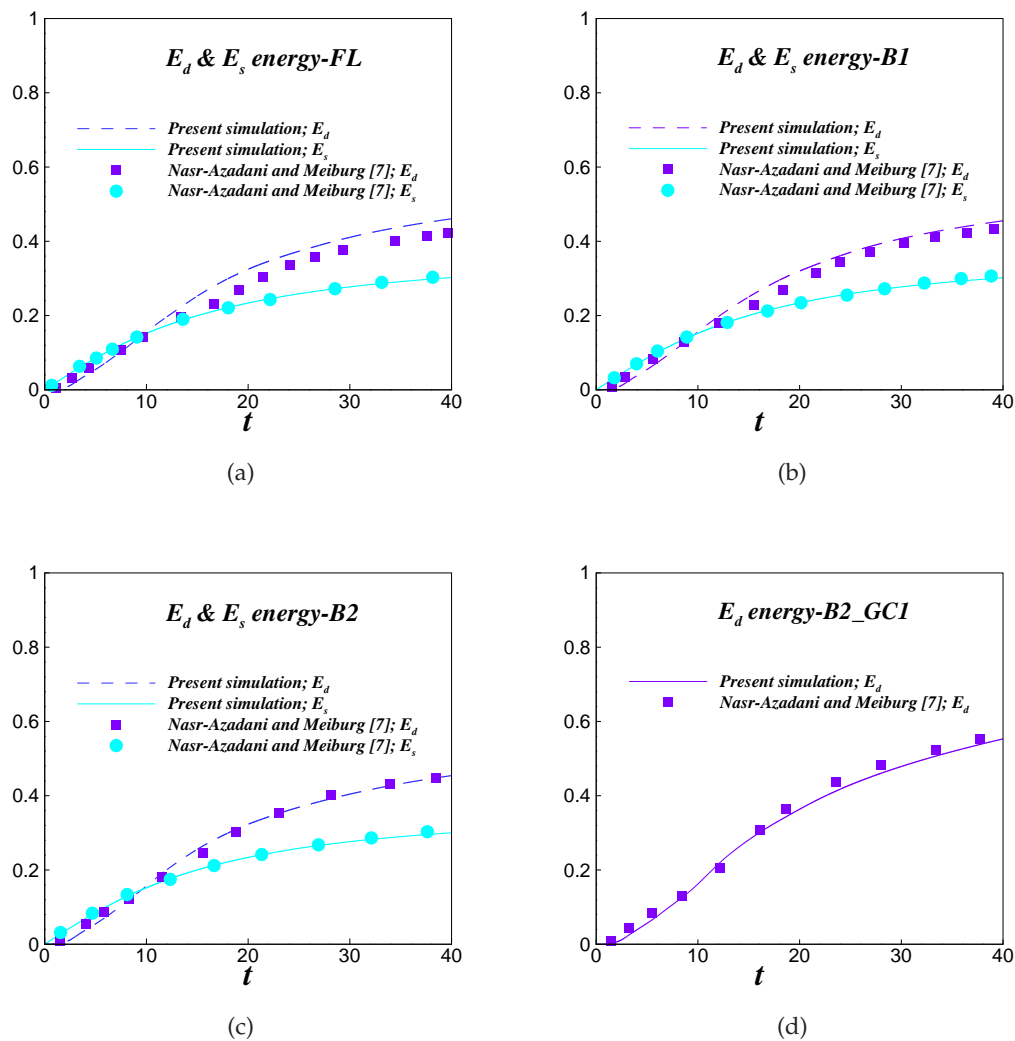
Figure 24: Time history of the predicted dissipation components E_d and E_s, which are compared with the numerical results of Nasr-Azadani and Meiburg [7]. (a) **FL**;(b) **B1**; (c) **B2**; (d) **B2**−**CG1**.

incompressible Navier-Stokes solutions. The predicted front location, suspended mass, sedimentation rate, and energy budget are all in good agreement with the simulated results using the direct numerical simulation model.

Acknowledgments

Appendix

Computation of the volume fraction of a solid (i.e. η) is necessary due to the interaction of fluid with the bump on the bottom surface (See Fig. 25). A reaction force will be generated from the bump. The center of a grid is defined in one cell at $(x_{i+\frac{1}{2},j+\frac{1}{2}}, y_{i+\frac{1}{2},j+\frac{1}{2}})$ and finer grids with spacings $\triangle x_1$ and $\triangle y_1$ are chosen to calculate the volume fraction of the bump. By defining $\frac{\triangle x}{\triangle x_1} = M$, $\frac{\triangle y}{\triangle y_1} = N$, the location of $x_{a,b}$ in one cell can be expressed as

$$x_{a,b} = \frac{1}{2}(x_{i-\frac{1}{2},j+\frac{1}{2}} + x_{i+\frac{1}{2},j+\frac{1}{2}}) + \frac{\triangle x_1}{2} + (a-1)\triangle x_1, \quad a=1,\cdots,M, \tag{A.1}$$

$$y_{a,b} = \frac{1}{2}(y_{i+\frac{1}{2},j-\frac{1}{2}} + y_{i+\frac{1}{2},j+\frac{1}{2}}) + \frac{\triangle y_1}{2} + (b-1)\triangle y_1, \quad b=1,\cdots,N, \tag{A.2}$$

where M,N denote the number of grid points in one cell along x,y-direction, respectively. The location $(x_{a,b}, y_{a,b})$ can be obtained from Eq. (A.1) and Eq. (A.2). The number of the points S in the solid region is then counted. Finally, the volume fraction of the bump of interest can be estimated as

$$\eta = \frac{S}{MN}. \tag{A.3}$$

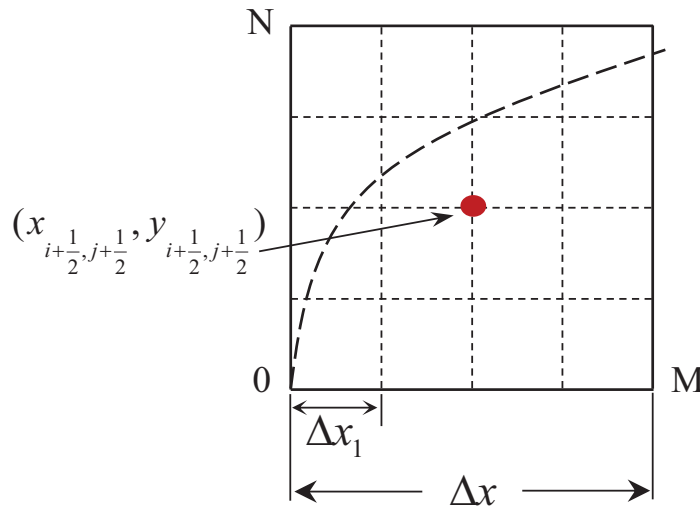Note that the values of M,N shown above are set to be 20.

Figure 25: Computation of the volume fraction of a solid. M,N denote the number of grid points in one cell along x,y-direction, respectively.

References

[1] J. E. Simpson, Gravity currents in the laboratory, atmosphere, and ocean, Annu. Rev. Fluid Mech., 14(1) (1982), 213-234.

[2] L. F. R. Espath, L. C. Pinto, S. Laizet and J. H. Silvestrini, Two- and three-dimensional direct numerical simulation of particle-laden gravity currents, Comput. Geosci., 63 (2014), 9-16.

[3] E. P. Francisco, L. F. R. Espath and J. H. Silvestrini, Direct numerical simulation of bi-disperse particle-laden gravity currents in the channel configuration, Appl. Math. Model, 49 (2017), 739-752.

[4] M. D. Patterson, J. E. Simpson, S. B. Dalziel and N. Nikiforakis, Numerical modelling of two-dimensional and axisymmetric gravity currents, Int. J. Numer. Meth. Fluids, 47(10-11) (2005), 1221-1227.

[5] M. M. Nasr-Azadani, E. Meiburg and B. Kneller, Mixing dynamics of turbidity currents interacting with complex seafloor topography, Environ. Fluid Mech., (2016), 1-23.

[6] M. M. Nasr-Azadani and E. Meiburg, Influence of seafloor topography on the depositional behavior of bidisperse turbidity currents: a three-dimensional, depth-resolved numerical investigation, Environ. Fluid Mech., 14(2) (2014a), 319-342.

[7] M. M. Nasr-Azadani and E. Meiburg, Turbidity currents interacting with three-dimensional seafloor topography, J. Fluid Mech, 745(2) (2014), 409-443.

[8] M. M. Nasr-Azadani, B. Hall and E. Meiburg E, Polydisperse turbidity currents propagating over complex topography: Comparison of experimental and depth-resolved simulation results, Comput. Geosci., 53 (2013), 141-153.

[9] F. Blanchette, V. Piche, E. Meiburg and M. Strauss, Evaluation of a simplified approach for simulating gravity currents over slopes of varying angles, Comput. Fluids, 35(5) (2006), 492-500.

[10] Y. J. Chou, S. H. Gu and Y. C. Shao, An Euler-Lagrange model for simulating fine particle suspension in liquid flows, J. Comput. Phys., 299 (2015), 955-973.

[11] Y. J. Chou, F. C. Wu and W. R. Shih, Toward numerical modeling of fine particle suspension using a two-way coupled Euler-Euler model-Part 1:Theoretical formulation and implications, Int. J. Multiphas. Flow, 64 (2014), 35-43.

[12] Y. J. Chou and Y. C. Shao, Numerical study of particle-induced Rayleigh-Taylor instability: Effects of particle settling and entrainment, Phys. Fluids, 28 (2016), 043302.

[13] G. Constantinescu, LES of lock-exchange compositional gravity currents: a brief review of some recent results, Springer Netherlands, 14(2) (2014), 295-317.

[14] M. M. Nasr Azadani and E. Meiburg, TURBINS: An immersed boundary, Navier Stokes code for the simulation of gravity and turbidity currents interacting with complex topographies, Comput. Fluids, 45(1) (2011), 14-28.

[15] F. Necker, C. Hartel, L. Kleiser and E. Meiburg, High resolution simulations of particle-driven gravity currents, Int. J. Multiphas. Flow, 28(2) (2002), 279-300.

[16] E. Meiburg and B. Kneller, Turbidity currents and their deposits, Annu. Rev. Fluid Mech., 42(1) (2010), 135-156.

[17] F. Blanchette, M. Strauss, E. Meiburg, B. Kneller and M. E. Glinsky, High-resolution numerical simulations of resuspending gravity currents: Conditions for self-sustainment, J. Geophys. Res., 110(C12) (2005).

[18] L. Lesshafft, E. Meiburg, B. Kneller and A. Marsden, Towards inverse modeling of turbidity currents: The inverse lock-exchange problem, Comput. Geosci., 37(4) (2011), 521-529.

[19] A. Harten, B. Engquist, S. Osher and S. R. Chakravarthy, Uniformly high order accurate

essentially non-oscillatory schemes, III, J. Comput. Phys., 71(2) (1987), 231-303.

[20] G. S. Jiang and C. W. Shu, Efficient implementation of weighted ENO schemes II, J. Comput. Phys., 126 (1996), 202-228.

[21] C. W. Shu, High order WENO and DG methods for time-dependent convection-dominated PDEs: A brief survey of several recent developments, J. Comput. Phys., 316 (2016), 598-613.

[22] X. Yu, J. J. Hsu and S. Balachandar, A spectral-like turbulence-resolving scheme for fine sediment transport in the bottom boundary layer, Comput. Geosci., 61 (2013), 11-22.

[23] S. K. Lele, Compact finite difference schemes with spectral-like resolution, J. Comput. Phys., 103(1) (1992), 16-42.

[24] Z. F. Tian, X. Liang and P. X. Yu, A higher order compact finite difference algorithm for solving the incompressible Navier-Stokes equations, Int. J. Numer. Meth. Eng., 88 (2011), 511-532.

[25] C. H. Yu, Y. G. Bhumkar and T. W. H. Sheu, Dispersion relation preserving combined compact difference schemes for flow problems, J. Sci. Comput,, 62(2) (2015), 482-516.

[26] P. H. Chiu and T. W H. Sheu, On the development of a dispersion-relation-preserving dual-compact upwind scheme for convection-diffusion equation, J. Comput. Phys., 228(10) (2009), 3640-3655.

[27] T. W. H. Sheu and C. H. Yu. Numerical simulation of free surface by an area-preserving level set method. Commun. Comput. Phys. 11(4) (2012), 1347-1371.

[28] C. H. Yu and T. W. H. Sheu. Simulation of incompressible free surface flow using the volume preserving level set method. Commun. Comput. Phys. 18(4) (2015), 931-956.

[29] C. H. Yu, D. Wang, Z. G. He and T. Pähtz, An optimized dispersion-relation-preserving combined compact difference scheme to solve advection equations, J. Comput. Phys., 300 (2015), 92-115.

[30] T. W. H. Sheu, H. F. Ting and R. K. Lin, An immersed boundary method for the incompressible Navier-Stokes equations in complex geometry, Int. J. Numer. Meth. Fluids, 56(7) (2008), 887-898.

[31] F. Gibou, R. P. Fedkiw, L. T. Cheng and M. Kang, A second-order-accurate symmetric discretization of the Poisson equation on irregular domains, J. Comput. Phys., 176(1) (2002), 205-227.

[32] E. Balaras, Modeling complex boundaries using an external force field on fixed Cartesian grids in large-eddy simulations, Comput. Fluids, 33(3) (2004), 375-404.

[33] P. H. Chiu, R. K. Lin and T. W. H. Sheu, A differentially interpolated direct forcing immersed boundary method for predicting incompressible Navier-Stokes equations in time-varying complex geometries, J. Comput. Phys., 229(12) (2010), 4476-4500.

[34] C. S. Peskin, Flow patterns around heart valves:A numerical method, J. Comput. Phys., 10(2) (1972), 252-271.

[35] M. J. Chern, D. Z. Noor, C. B. Liao and T. L. Horng, Direct-forcing immersed boundary method for mixed heat transfer, Commun. Comput. Phys., 18(4) (2015), 1072-1094.

[36] S. Osher, R. Fedkiw and K. Piechor, Level set methods and dynamic implicit surfaces, Appl. Mech. Rev., 57(3) (2004), B15.

[37] H. Q. Wang and Y. Xiang, An adaptive level set method based on two-level uniform meshes and its application to dislocation dynamics, Int. J. Numer. Meth. Eng., 94 (2013), 573-597.

[38] F. Necker, C. Hartel, L. Kleiser and E. Meiburg, Mixing and dissipation in particle-driven gravity currents, J. Fluid Mech., 541(1) (2005), 339-372.

[39] E. A. Fadlun, R. Verzicco, P. Orlandi and J. Mohd-Yusof, Combined immersed-boundary finite-difference methods for three-dimensional complex flow simulations, J. Comput. Phys.,

161 (2000), 35-60.

[40] D. Pan and C. H. Chang, The capturing of free surfaces in incompressible multi-fluid flows, Int. J. Numer. Meth. Fluids, 30 (2000), 203-222.

[41] F. Xiao and A. Ikebata, An efficient method for capturing free boundaries in multi-fluid simulations, Int. J. Numer. Meth. Fluids, 42 (2003), 187-210.

[42] F. Xiao, Y. Honma and T. Kono, A simple algebraic interface capturing scheme using hyperbolic tangent function, Int. J. Numer. Meth. Fluids, 48(9) 2003, 1023-1040.

[43] K. M. Shyue, F. Xiao , An Eulerian interface sharpening algorithm for compressible two-phase flow: The algebraic THINC approach, J. Comput. Phys., 268 (2014), 326-354.

[44] S. Ii, K. Sugiyama, S. Takeuchi, S. Takagi, Y. Matsumoto and F. Xiao, An interface capturing method with a continuous function: the THINC method with multi-dimensional reconstruction, J. Comput. Phys., 231(5) 2012, 2328-2358.

[45] M. Sussman and E. Fatemi, An efficient interface-preserving level set redistancing algorithm and its application to interfacial incompressible fluid flow, SIAM J. Sci. Comput., 20(4) (1999), 1165-1191.

[46] K. Yokoi, A variational approach to motion of triple junction of gas, liquid and solid, Comput. Phys. Communi., 180(7) (2009), 1145-1149.

[47] G. S. Jiang and D. Peng, Weighted ENO schemes for Hamilton-Jacobi equations, SIAM J. Sci. Comput., 21(6) (2000), 2126-2143.

[48] Y. Zhang, Q. Zou and D. Greaves, Numerical simulation of free-surface flow using the level-set method with global mass correction, Int. J. Numer. Meth. Fluids, 63(6) 2010, 651-680.

[49] Y. Zhang, Q. Zou, D. Greaves, D. Reeve, A. Hunt-Raby, D. Graham, P. James and X. Lv, A level set immersed boundary method for water entry and exit, Commun. Comput. Phys., 8(2) (2010), 265-288.

[50] C. W. Shu and S. Osher, Efficient implementation of essentially non-oscillatory shock-capturing schemes II, J. Sci. Comput., 83(1) (1989),32-78.

[51] P. C. Chu and C. Fan, A three-point combined compact difference scheme, J. Sci. Comput., 140(2) (1998), 370-399.

[52] W. J. Minkowycz and E. M. Sparrow, Advances in Heat Transfer, 2000,(1).

[53] A. J. Chorin, Numerical solution of the Navier-Stokes equations, Comput. Fluid Mech., 22(104) (1968), 745-762.

[54] T. Bonometti and S. Balachandar, Effect of Schmidt number on the structure and propagation of density currents, Theor. Comput. Fluid Dyn, 22 (2008), 341-361.

[55] J. W. Rottman and J. E. Simpson, Gravity currents produced by instantaneous releases of a heavy fluid in a rectangular channel, J. Fluid Mech., 135(1) (1983), 95-110.

[56] H. E. Huppert and J. E. Simpson, The slumping of gravity currents, J. Fluid Mech., 99(4) (1980), 785-799.